

Non-Heme Diiron Model Complexes Can Mediate Direct NO Reduction: Mechanistic Insight Into Flavodiiron NO Reductases

Hai Dong, Corey J. White, Bo Zhang, Carsten Krebs, and Nicolai Lehnert

J. Am. Chem. Soc., **Just Accepted Manuscript** • DOI: 10.1021/jacs.8b08567 • Publication Date (Web): 17 Sep 2018

Downloaded from <http://pubs.acs.org> on September 17, 2018

Just Accepted

“Just Accepted” manuscripts have been peer-reviewed and accepted for publication. They are posted online prior to technical editing, formatting for publication and author proofing. The American Chemical Society provides “Just Accepted” as a service to the research community to expedite the dissemination of scientific material as soon as possible after acceptance. “Just Accepted” manuscripts appear in full in PDF format accompanied by an HTML abstract. “Just Accepted” manuscripts have been fully peer reviewed, but should not be considered the official version of record. They are citable by the Digital Object Identifier (DOI®). “Just Accepted” is an optional service offered to authors. Therefore, the “Just Accepted” Web site may not include all articles that will be published in the journal. After a manuscript is technically edited and formatted, it will be removed from the “Just Accepted” Web site and published as an ASAP article. Note that technical editing may introduce minor changes to the manuscript text and/or graphics which could affect content, and all legal disclaimers and ethical guidelines that apply to the journal pertain. ACS cannot be held responsible for errors or consequences arising from the use of information contained in these “Just Accepted” manuscripts.

1
2
3
4
5
6
7
8
9
10
11
12

Non-Heme Diiron Model Complexes Can Mediate Direct NO Reduction: Mechanistic Insight Into Flavodiiron NO Reductases

13 Hai T. Dong,^a Corey J. White,^a Bo Zhang,^b Carsten Krebs,^b Nicolai Lehnert^{a,*}

14 ^a Department of Chemistry, The University of Michigan, Ann Arbor, Michigan 48109-1055,
15 United States

16 ^b Department of Chemistry and Department of Biochemistry and Molecular Biology, The
17 Pennsylvania State University, University Park, Pennsylvania 16802, United States
18
19
20
21
22
23
24
25
26
27
28
29
30
31
32
33
34
35
36
37
38
39
40
41
42
43
44
45
46
47
48
49
50
51
52
53
54
55
56
57
58
59
60

Abstract:

Flavodiiron nitric oxide reductases (FNORs), a common enzyme family found in various types of pathogenic bacteria, are capable of reducing nitric oxide (NO) to nitrous oxide (N₂O) as a protective detoxification mechanism. Utilization of FNORs in pathogenic bacteria helps them survive and proliferate in the human body, thus causing chronic infections. In this paper, we present a new diiron model complex, [Fe₂((Py₂PhO₂)MP)(OPr)₂](OTf) with bridging propionate ligands (OPr) that is capable of directly reducing NO to N₂O in quantitative yield without the need to (super)reduce the complex. We first prepared the diferric precursor and characterized it by UV-Vis, IR, NMR and Mössbauer spectroscopies, cyclic voltammetry, and mass spectrometry. This complex can then conveniently be reduced to the diferrous complex using CoCp₂. Even though this diferrous complex is highly reactive, we have successfully isolated and characterized this species using X-ray crystallography and various spectroscopic techniques. *Most importantly, upon reacting this diferrous complex with NO gas, we observe quantitative formation of N₂O via IR gas headspace analysis, the first demonstration of direct NO reduction by a non-heme diiron model complex.* This finding directly supports recent mechanistic proposals for FNORs.

1. Introduction

Nitric oxide (NO) is ubiquitous in biological systems and serves, for example, as a signaling molecule that regulates blood pressure and is involved in nerve signal transduction in mammals at low, nanomolar concentrations.¹⁻³ Higher concentrations of NO are acutely toxic and are used by mammals for immune defense.⁴ Recent research has shown that some pathogens (e.g. *Escherichia coli*, *Trichomonas vaginalis*, etc.) have evolved a defense system against NO toxicity by sensing NO and subsequently expressing flavodiiron nitric oxide reductases (FNORs) as a response to nitrosative stress.⁵⁻⁷ These enzymes are able to efficiently remove NO by reducing it to less toxic N₂O. As a result, harmful pathogens can proliferate in the human body, causing chronic infections. Because of this, FNORs are potential targets for the development of new therapeutics, especially against drug resistant strains.

FNORs belong to the family of flavodiiron proteins (FDPs), which were first recognized for their function as O₂ scavengers, protecting microanaerobically living organisms against residual O₂.⁸ These enzymes are usually homodimers. Each subunit contains an N-terminal non-heme diiron active site and a C-terminal Flavin binding domain. In the head-to-tail arrangement of the homodimer, the non-heme diiron core of one subunit is then close to the Flavin mononucleotide (FMN) cofactor of the adjacent subunit.⁹ The non-heme diiron centers of FDPs, which are ligated by histidine and carboxylate side chains and a bridging hydroxide ligand,¹⁰ show Fe-Fe distances of 3.2 - 3.6 Å (see Figure 1). One key difference to other non-heme diiron enzymes like soluble methane monooxygenase (sMMO) and ribonucleotide reductases (RRs) is the presence of the redox-active FMN cofactor in close proximity (4 - 6 Å) to the diiron active site of FDPs. Recent single turnover experiments by Kurtz and coworkers on the FDP from *Thermotoga maritima* have provided strong evidence for a direct NO reduction pathway via the formation of an antiferromagnetically (AF) coupled high-spin (hs) diferrous dinitrosyl intermediate (or [$\{hs\text{-FeNO}\}^7$]₂ in the Enemark-Feltham notation, where the exponent “7” corresponds to the number of Fe(d) and NO(π^*) electrons¹¹).¹²⁻¹⁴ In this mechanistic scenario, the FMN would not directly participate in the NO reduction process, but would only be important to reduce the diiron core back to the diferrous form after turnover, as shown in Scheme 1, top.¹³ Based on these important results, the diferrous dinitrosyl complex has now been established as the catalytically competent intermediate that is formed prior to N₂O release,¹² which rules out other mechanistic proposals based on a reactive mononitrosyl adduct.^{8,12} This direct NO reduction

1
2
3 pathway requires that the $[\{\text{hs-FeNO}\}^7]_2$ intermediate is capable of coupling the two NO ligands
4 and reducing them to N_2O without the addition of any extra electrons, *a reaction that is*
5 *unprecedented in non-heme diiron NO chemistry*. Since the *T. maritima* FDP is an O_2 reducing
6 enzyme, it is not clear at this point, however, if FNORs use the same pathway to reduce NO under
7 turnover conditions.
8
9
10

11
12 In contrast to these findings for FDPs, mono- and dinuclear $\{\text{FeNO}\}^7$ model complexes are
13 generally stable, and no direct N_2O formation from these complexes has been reported.¹⁵ Most
14 recently, a new mechanism of N-N coupling has been observed by our group for the model
15 complex $[\text{Fe}_2(\text{BPMP})(\text{OPr})(\text{NO})_2](\text{X})_2$ ($\text{H}[\text{BPMP}] = 2,6\text{-bis}[[\text{bis}(2\text{-pyridylmethyl})\text{amino}]\text{methyl}]\text{-}$
16 4-methylphenol , see Figure 2c; $\text{OPr}^- = \text{propionate bridging ligand}$, $\text{X}^- = \text{BPh}_4^-, \text{OTf}^-$), which is
17 the first functional model system for FNORs. This $[\text{hs-}\{\text{FeNO}\}^7]_2$ complex is stable and has been
18 structurally and spectroscopically characterized.¹⁶ Upon one electron reduction, however, the
19 complex shows very fast ($k_{\text{obs}} > 100 \text{ s}^{-1}$) and quantitative N_2O formation, using the semireduced
20 mechanism shown in Scheme 1, bottom.¹⁷ Computational results indicate that the critical step of
21 the reaction is the first step, the N-N bond formation.¹⁸ By reducing one of the $\{\text{hs-FeNO}\}^7$ units
22 to $\{\text{hs-FeNO}\}^8$, $[\text{Fe}_2(\text{BPMP})(\text{OPr})(\text{NO})_2](\text{X})_2$ is activated for N-N coupling, generating an N-
23 bound, bridging *cis*-hyponitrite intermediate. After rearrangement to the $\kappa^2\text{-O}_2\text{N}_2^{2-}$ binding mode,
24 N_2O is generated with a small activation barrier of only 5.6 kcal/mol in free energy for N-O bond
25 cleavage. The semireduced mechanism is therefore a very efficient pathway for N_2O formation
26 from a diiron core.
27
28
29
30
31
32
33
34
35
36
37

38 A third possibility for N_2O formation from the $[\text{hs-}\{\text{FeNO}\}^7]_2$ intermediate is the super-
39 reduced mechanism, according to Scheme 1, middle. Recently, two unique mononitrosyl model
40 complexes have been reported and have been proposed to mediate N_2O formation via this
41 mechanism. Here, the $\{\text{hs-FeNO}\}^7$ centers are reduced to $\{\text{hs-FeNO}\}^8$ before N_2O formation
42 occurs. Jana et al. uses a very innovative approach to access a dimeric mononitrosyl complex by
43 reacting the precursor, $[\text{Fe}_2(\text{N-Et-HPTB})(\text{CH}_3\text{COS})](\text{BF}_4)_2$, with $(\text{NO})(\text{BF}_4)$ (Figure 2a).¹⁹ This
44 mononitrosyl complex can carry out quantitative N_2O formation within 15 minutes after one
45 reductive equivalent (per diiron mononitrosyl complex) is added. Confer et al., on the other hand,
46 have used a pentadentate ligand scaffold with a thiolate, denote as N3PySH , to generate an $\{\text{hs-}$
47 $\text{FeNO}\}^7$ complex that can be reduced to generate an $\{\text{hs-FeNO}\}^8$ species (Figure 2b).²⁰ This $\{\text{hs-}$
48 $\text{FeNO}\}^8$ complex then undergoes a self-decay process over 20 hours to form N_2O with 54% yield.
49
50
51
52
53
54
55
56
57
58
59
60

1
2
3 Albeit slow in reactivity, this mononuclear complex also supports the feasibility of the proposed
4 superreduced mechanism for FNORs. In both Jana's and Confer's compounds, however, the
5 reaction has to proceed via an intermolecular N-N coupling process, which is different from the
6 enzyme and also the model complex $[\text{Fe}_2(\text{BPMP})(\text{OPr})(\text{NO})_2](\text{X})_2$.
7
8
9

10 In summary, even though evidence for the direct NO reduction pathway has been presented
11 for FDPs, no synthetic model complex has been able to mediate this reaction so far, and hence, the
12 feasibility of this process is still in question. Based on our results for $[\text{Fe}_2(\text{BPMP})(\text{OPr})(\text{NO})_2](\text{X})_2$
13 and the ability of this complex to mediate N_2O formation via the semireduced pathway, we
14 hypothesized that a complex with more reducing iron centers might allow for the direct reduction
15 of NO to N_2O from the $[\{\text{FeNO}\}^7]_2$ intermediate. To test the feasibility of this idea, we prepared
16 the model complex $[\text{Fe}^{\text{III}}_2((\text{Py}_2\text{PhO}_2)\text{MP})(\text{OPr})_2](\text{OTf})$ (**1**) where two of the pyridine groups in the
17 H-BPMP ligand used previously are replaced by more electron-donating phenolate groups (Figure
18 3). Complex **1** was characterized through spectroscopic methods and electrochemical studies. This
19 complex can be reduced (using CoCp_2) to the diferrous complex (**2**), which was structurally
20 characterized using X-ray crystallography. Excitingly, the reduced complex produces N_2O in
21 quantitative yield when reacted with NO, making (**2**) the first model complex that is capable of
22 mimicking the direct reduction of NO to N_2O as proposed for FNORs.¹³ Additionally, the products
23 after reduction of NO to N_2O at both room temperature and $-80\text{ }^\circ\text{C}$ were spectroscopically
24 characterized, providing further insight into the mechanism of N_2O generation by **2**.
25
26
27
28
29
30
31
32
33
34
35
36
37

38 2. Experimental Section

39
40 Reactions were generally performed using inert gas (Schlenk) techniques. All solvents were
41 dried and freeze pump thawed to remove dioxygen and water. Preparation and handling of air
42 sensitive materials was performed under a dinitrogen atmosphere in an MBraun glovebox,
43 equipped with a circulating purifier (O_2 , $\text{H}_2\text{O} < 0.1$ ppm). Nitric oxide (99.95%) was first passed
44 through an Ascarite II column and then a $-80\text{ }^\circ\text{C}$ cold trap to remove higher nitrogen oxide
45 impurities prior to use.
46
47
48
49

50 **Infrared spectra** of solid samples were obtained using PerkinElmer BX and GX and Bruker
51 Alpha-E FTIR spectrometers. The IR spectra of solution samples were obtained in thin-layer
52 solution cells equipped with CaF_2 windows. Gas IR spectra were obtained using a Pike
53
54
55
56
57

Technologies short-path HT gas cell with 100 mm path length, equipped with CaF₂ windows, on the same instruments.

UV-Vis/Immersion Probe: Spectra were obtained using an Analytic Jena Specord S600 UV-Vis spectrometer. Dip probe experiments used the same spectrometer, with a Helma low-temperature immersion probe.

¹H-NMR spectra were recorded on a Varian Inova 400 MHz instrument and referenced against residual solvent signals.

Electron paramagnetic resonance spectra were recorded on a Bruker-X-band EMX spectrometer equipped with Oxford Instruments liquid nitrogen and liquid helium flow cryostats. EPR spectra were typically obtained on frozen solutions using ~20 mW microwave power and 100 kHz field modulation with the amplitude set to 1 G. Sample concentrations were ~2 mM, and ~4 mM for reaction products.

Cyclic voltammograms (CVs) were obtained on a CH instruments CHI660C electrochemical workstation using a three component system, consisting of a glassy carbon working electrode, a platinum auxiliary electrode, and a Ag wire reference electrode. CVs were recorded in 0.1 M tetrabutylammonium triflate in CH₂Cl₂. Potentials were corrected to the Fc/Fc⁺ standard by independently measuring the ferrocene/ferrocenium couple under the same conditions (Fc/Fc⁺ = 624 mV vs. SHE).

Elemental analysis: Elemental analyses were conducted by Atlantic Microlabs (Norcross, GA)

Structure Determination. Orange rods of [Fe₂((Py₂PhO₂)MP)(OAc)₂](CoCp₂) (2-OAc) were grown from a dichloromethane/hexane solution of the compound at 25 °C. A crystal of dimensions 0.20 x 0.05 x 0.05 mm was mounted on a Rigaku AFC10K Saturn 944+ CCD-based X-ray diffractometer equipped with a low temperature device and a Micromax-007HF Cu-target micro-focus rotating anode ($\lambda = 1.54187 \text{ \AA}$), operated at 1.2 kW power (40 kV, 30 mA). The X-ray intensities were measured at 85(1) K with the detector placed at a distance of 42.00 mm from the crystal. A total of 2028 images were collected with an oscillation width of 1.0° in ω . The exposure times were 1 sec. for the low angle images, and 4 sec. for high angle. Rigaku d*trek images were exported to CrysAlisPro for processing and corrected for absorption. The integration of the data yielded a total of 83840 reflections to a maximum 2 θ value of 139.83° of which 10012 were independent and 8304 were greater than 2 σ (I).^{21,22} The final cell constants (Table S1) were

1
2
3 based on the xyz centroids of 17825 reflections above $10\sigma(I)$. Analysis of the data showed
4 negligible decay during data collection. The structure was solved and refined with the Bruker
5 SHELXTL (version 2016/6)²³ software package, using the space group C2/c with $Z = 8$ for the
6 formula $C_{51}H_{53}N_{40}O_{7}Cl_{4}Fe_2Co + CH_2Cl_2$. All non-hydrogen atoms were refined anisotropically
7 with the hydrogen atoms placed in idealized positions. Full matrix least-squares refinement based
8 on F2 converged at $R1 = 0.0553$ and $wR2 = 0.1500$ [based on $I > 2\sigma(I)$], $R1 = 0.0668$ and
9 $wR2 = 0.1616$ for all data. Two dichloromethane solvate molecules were disordered in two
10 orientations but were able to be refined with discrete atomic positions. The SQUEEZE subroutine
11 of the PLATON program suite^{24,25} was used to address additional disordered solvent present in
12 four accessible voids of the lattice. Further details are presented in Table S1 and are given as
13 Supporting Information in a CIF file.

14
15
16
17
18
19
20
21
22 **Mössbauer spectroscopy.** The Mössbauer sample of **1** was prepared by metallating the ligand,
23 $H_3[(Py_2PhO_2)MP]$, with $^{57}Fe(OTf)_3$ in the presence of NaOPr (see below). The subsequent
24 preparation of samples of **2** and of the reaction products was carried out using **1** as precursor.
25 Samples were dissolved in butyronitrile and then slowly frozen at liquid nitrogen temperature in a
26 cold well under a dinitrogen atmosphere.

27
28
29
30
31 Mössbauer data were recorded on a spectrometer from WEB Research, equipped with a Janis
32 SVT-400 variable-temperature cryostat. All isomer shifts are quoted relative to the centroid of the
33 spectrum of α -Fe at room temperature. Simulation of the Mössbauer spectra was conducted with
34 the WMOSS spectral analysis package, using the Spin Hamiltonian shown in the following
35 equation:

$$36 \mathbf{H} = \beta \mathbf{S} \cdot \mathbf{g} \cdot \mathbf{B} + D \left(\mathbf{S}_z^2 - \frac{S(S+1)}{3} \right) + E(\mathbf{S}_x^2 - \mathbf{S}_y^2) + \frac{eQV_{zz}}{4} \left[\mathbf{I}_z^2 - \frac{I(I+1)}{3} + \frac{\eta}{3} (\mathbf{I}_x^2 - \mathbf{I}_y^2) \right]$$

$$37 + \mathbf{S} \cdot \mathbf{A} \cdot \mathbf{I} - g_n \beta_n \mathbf{B} \cdot \mathbf{I}$$

38
39
40
41
42
43
44 The first term represents the electronic Zeeman effect, the second and third term represent the axial
45 and rhombic zero field splitting (ZFS), the fourth term describes the interaction between the
46 nuclear quadrupole moment and the electric field gradient, the fifth term represents the magnetic
47 hyperfine interaction of the electronic spin with the ^{57}Fe nucleus, and the last term describes the
48 ^{57}Fe nuclear Zeeman effect.

49
50
51
52 **DFT calculations.** Gaussian 09 was used to carry out all of the calculations performed here.²⁶
53 The optimization of the broken symmetry structure of the diferrous dinitrosyl intermediate,
54 $[Fe_2((Py_2PhO_2)MP)(OPr)(NO)_2]$, was performed with the gradient corrected functional BP86,
55

1
2
3 which has been shown to give good geometric structures for related $\{MNO\}^n$ species,¹⁸ and the
4 TZVP basis set. A guess calculation is performed first on the ferromagnetically coupled state of
5 the dimer, and used as the initial guess to generate the broken-symmetry wavefunction. Subsequent
6 single point calculations during the geometry optimization were carried out to ensure that the two
7 iron centers remain antiferromagnetically coupled (and are not spin quenched). A frequency
8 calculation was further performed on the optimized structure to determine the N-O stretching
9 frequencies.

15 **2,6-Bis[(2-hydroxybenzyl)(2-pyridylmethyl)amino)methyl]-4-methylphenol**

16 (H₃[(Py₂PhO₂)MP], H₃L). H₃L was synthesized according to published procedures.²⁷ ¹H-NMR
17 (400 MHz, Chloroform-*d*) δ 10.83 (s, 3H), 8.63 (d, 2H), 7.65 (td, 2H), 7.26 – 7.19 (m, 4H), 7.17 –
18 7.11 (m, 2H), 7.03 (d, 2H), 6.87 (s, 2H), 6.81 (d, 2H) 6.75 (td, 2H), 3.83 (s, 4H), 3.80 (s, 4H), 3.75
19 (s, 4H), 2.21 (s, 3H); see Figure S38.

20
21
22
23
24 **[Fe₂((Py₂PhO₂)MP)(OPr)₂](OTf)•H₂O (1)**. To a solution of 0.1 g (0.178 mmol) of H₃L in
25 2 ml of Methanol, a solution of 100 mg (1.03 mmol) sodium propionate (denote as NaOPr) in 1
26 ml of MeOH was added. A solution of 155.7 mg (0.356 mmol) Fe(OTf)₂•2CH₃CN in 1 mL of
27 methanol was then added to the stirring solution. The resulting solution was stirred for 30 minutes
28 at 50 °C under ambient conditions and then filtered. The crude solid was washed with 2-propanol
29 and diethyl ether until the filtrate is colorless to obtain the product as a dark blue solid; yield:
30 0.134g, 77%. Characterization: Elemental anal. calcd. for C₄₂H₄₃Fe₂F₃N₄O₁₀S: C, 51.34; H, 4.62;
31 N, 5.70; found (1st attempt) (%):C, 51.07; H, 4.57; N, 5.50 (2nd attempt) (%):C, 51.56; H, 4.68; N,
32 5.82. Mass spectroscopy m/z: calcd. for the cationic fragment C₄₁H₄₃Fe₂N₄O₇: 815.18; Found:
33 815.19. Mass spectroscopy m/z: calcd. for the ⁵⁷Fe labeled cationic fragment C₄₁H₄₃⁵⁷Fe₂N₄O₇:
34 817.18; Found: 817.19 UV-Vis (CH₂Cl₂) (λ_{max}) 630 nm.

35
36
37
38
39
40
41
42
43 **[Fe₂((Py₂PhO₂)MP)(OPr)₂](ClO₄)•H₂O (1/ClO₄)**. A similar procedure was used as in the
44 case of **1**, but the metalation was performed with Fe(ClO₄)₂ under ambient conditions.
45 Characterization: Elemental anal. calcd. for C₄₂H₄₃Fe₂N₄O₁₁Cl: C, 52.78; H, 4.86; N, 6.01; found
46 (%):C, 53.29; H, 4.85; N, 5.99.

47
48
49
50 **[Fe₂((Py₂PhO₂)MP)(OAc)₂](ClO₄)•H₂O (1-OAc)**. This complex was prepared and
51 characterized according to a previously reported procedure.²⁸
52
53
54
55
56
57
58
59
60

1
2
3
4
5
6
7
8
9
10
11
12
13
14
15
16
17
18
19
20
21
22
23
24
25
26
27
28
29
30
31
32
33
34
35
36
37
38
39
40
41
42
43
44
45
46
47
48
49
50
51
52
53
54
55
56
57
58
59
60

Complex **2** and **2-OAc** can be obtained through chemical reduction of **1** and **1-OAc**, respectively, using cobaltocene. Single crystals of **2-OAc** suitable for X-ray crystallography were grown by diffusion of hexane into a CH₂Cl₂ solution of the compound.

IR Gas Headspace Analysis for N₂O Detection. N₂O quantification was carried out by gas headspace analysis using infrared spectroscopy. The general protocol for gas headspace analysis is described in the following (taken from ref. ²⁹): to a sealed 25 ml round-bottom flask containing ~8.7 mg of [Fe₂((Py₂PhO₂)MP)(OPr)₂](OTf) in 2.5 mL of CH₂Cl₂ were added ~2 equivalents of CoCp₂. After allowing the reduction to proceed, ~2 mL of NO gas were added into the headspace of the round-bottom flask. The reaction was allowed to stir for 15 minutes before the headspace was transferred by vacuum to a sealed gas IR cell with CaF₂ windows. Quantification of N₂O was performed via integration of the prominent IR features at 2235 and 2212 cm⁻¹ of this molecule (N-N stretching vibration) against separately determined N₂O standards, which were generated from the breakdown of Piloty's acid in basic solution under exactly the same conditions. Using this calibration method, a maximum N₂O yield of 105% ± 10% was obtained for **1**, as shown in Figure S25. The advantage of using Piloty's acid to construct the calibration curve is that this compound is a solid that can be weighted out at high accuracy. Hence, exact amounts of N₂O can be generated in this way. The disadvantage is that Piloty's acid has to be used in an aqueous environment, which is different from the organic solvents used for the reaction of **2** with NO gas. However, the error generated due to the somewhat different solubility of N₂O in water and organic media (at the concentrations used for the experiments) is well within the ± 10% error noted above.

Additional Control Experiments. As an additional control, NO-saturated CH₂Cl₂ was exposed to cobaltocene under identical conditions to those used for N₂O generation from the reaction of **2** with NO gas. While cobaltocene is able to reduce NO (NO is reduced around -1 V versus Fc/Fc⁺ in organic solvents), the rate for N₂O generation and total percent yield differ greatly from those observed for **2**.¹⁶ In addition, we are adding exactly two equivalents of CoCp₂ to the solution of **1** to generate **2** (prior to reaction with NO gas), so the amount of free CoCp₂ present in solution at the time when NO gas is added is minute, if there is any present at all. A direct reduction of NO by CoCp₂ can therefore be ruled out in our experiments.

3. Results and Discussion

The ligand $H_3[(Py_2PhO_2)MP]$ (also referred to as $H_3[BBPMP]$ in the literature) was synthesized using a reported procedure and characterized by 1H -NMR spectroscopy.²⁷ Complexes **2** and **2-OAc** are difficult to generate in pure form and store, due to their high oxygen sensitivity. Because of this, we decided to prepare the diferric precursor first, and then simply reduce it to the diferrous form *in situ*, right before performing reactivity studies.²⁸ We prepared several derivatives of the diferric complex, with different bridging carboxylate ligands and counter ions, to demonstrate the consistency of the NO reduction reaction across all of these different derivatives (see Scheme 2, also for the numbering scheme of our complexes).

3.1 Synthesis and spectroscopic characterization of complexes **1** and **2**

Synthesis of the diferric complex $[Fe^{III}_2((Py_2PhO_2)MP)(OPr)_2](OTf)$ (**1**) was accomplished by reaction of $Fe(OTf)_2$ with the ligand in the presence of excess $NaOPr$ (OPr^- = propionate) under ambient condition. The analogous complexes with acetate (OAc^-) bridges, $[Fe^{III}_2((Py_2PhO_2)MP)(OAc)_2](OTf)$ (**1-OAc**), and the corresponding perchlorate salts were also prepared (the latter for X-ray crystallography) for comparison. The deep-blue complex **1** is characterized by a broad absorption band at 630 nm ($\epsilon = 6840 M^{-1}cm^{-1}$, in CH_2Cl_2) as shown in Figure 4. 1H -NMR spectroscopy in CD_2Cl_2 shows signals ranging from -10 to 50 ppm (Figure S34). The wide range of chemical shifts as well as the broad nature of the features are an indication of paramagnetic iron centers. The Mössbauer spectrum of complex **1** shows a quadrupole doublet with an isomer shift $\delta = 0.54$ mm/s and a quadrupole splitting parameter $\Delta E_Q = 1.10$ mm/s (Figure 5). These parameters are consistent with an antiferromagnetically (AF) coupled high-spin diferric complex, and they are also in agreement with the Mössbauer parameters of the **1-OAc** complex, which have previously been reported ($\delta = 0.54$ mm/s, $\Delta E_Q = 1.06$ mm/s).²⁸ Indeed, magnetic susceptibility measurement of **1-OAc** show weak AF coupling between the Fe centers, with a reported coupling constant $J = -6.0 (\pm 1) cm^{-1}$. X-band electron paramagnetic resonance (EPR) spectroscopy of **1** at 4 K in frozen CH_2Cl_2 solution further reveals that **1** is EPR silent, in agreement with these results.

Interestingly, previous studies have shown that by replacing a pyridine on the H-BPMP ligand by one phenolate group, the redox potential of the diiron complex is shifted by approximately 500 mV.³⁰ To assess the redox properties of our complex, the cyclic voltammogram (CV) of complex **1** in dichloromethane (CH_2Cl_2) was recorded by scanning negatively from the

1
2
3 open circuit potential at various scan rates. The resulting CVs of **1** are shown in Figure 6. Two
4 reversible redox couples are observed with $E_{1/2}$ of -0.28 V and -1.0 V versus Fc^+/Fc . These
5 correspond to the Fe^{III}/Fe^{III} to Fe^{III}/Fe^{II} and Fe^{III}/Fe^{II} to Fe^{II}/Fe^{II} couples, respectively. *Importantly,*
6 *compared to complex $[Fe_2(BPMP)(OPr)_2](OTf)$ studied previously, these redox potentials are*
7 *negatively shifted by about 1 V, demonstrating that our goal to prepare a more electron-rich analog*
8 *of the $BPMP^-$ complex has been accomplished.* Compared to FNORs, complex **1** shows a more
9 negative redox potential of about 300 mV.^{31,32}

10
11
12
13
14
15 The diferrous state of **1-OAc**, denote here as **2-OAc**, has been reported to be unstable and
16 thus prevented further spectroscopic and structural characterization in a previous report.²⁸ In this
17 work, however, we show that complex **1** can conveniently be reduced to the diferrous complex **2**
18 *in situ* by addition of exactly 2 equivalents of cobaltocene ($CoCp_2$), as illustrated by a
19 corresponding redox titration (Figures S2-S3). The reduction leads to the disappearance of the 630
20 nm band of **1**, and a smaller band appears at 530 nm ($\epsilon = 2620 M^{-1}cm^{-1}$, in CH_2Cl_2) indicating the
21 formation of **2** (Figure 4). This goes along with a characteristic color change of the solution from
22 dark blue to dark orange. The Mössbauer spectrum of **2** (Figure 5) shows a quadrupole doublet
23 with $\delta = 1.25$ mm/s and $\Delta E_Q = 2.97$ mm/s, consistent with a high-spin diferrous complex. X-band
24 EPR spectroscopy of **2** at 4 K in frozen CH_2Cl_2 solution reveals that **2** is EPR silent, as expected.
25 Note that complex **2** can also be accessed by direct reaction of $H_3[(Py_2PhO_2)MP]$ with $Fe(OTf)_2$
26 in the presence of base and the bridging propionate ($NaOPr$), but, as mentioned above, it is
27 advantageous to enter this chemistry via the diferric complex **1**, which is much more stable.
28 Interestingly, complex **2** shows an unexpected temperature-dependent property where it changes
29 color from deep orange to very faint yellow (almost no color) when a solution of this compound
30 is cooled down from room temperature to -80 °C in dichloromethane. The absorption band at 530
31 nm disappears as the temperature decreases, and the resulting absorption spectrum shows just a
32 weak feature at ~500 nm (Figure S4, top). We hypothesize that in solution, the bridging propionate
33 ligands of complex **2** are fluxional, such that at room temperature, these ligands can dissociate
34 (partly or completely) to form five-coordinate iron centers. As the temperature is decreased, the
35 propionates (either dissociated or still bound as monodentate ligands) rebind to the iron centers
36 (driven by entropy), forming six-coordinate Fe(II) centers with two bridging propionates at -80 °C.
37 This hypothesis is supported by the crystal structure of **2-OAc** and the Mössbauer spectra of the
38 reaction product of **2** with NO at -80 °C.
39
40
41
42
43
44
45
46
47
48
49
50
51
52
53
54
55
56
57
58
59
60

3.2 Structural comparison of complexes **1-OAc** and **2-OAc**

Structural characterization of complex **1** has proven to be challenging due to the high degree of disorder caused by the $-\text{CH}_2\text{CH}_3$ groups of the bridging propionate ligands, and further disorder introduced by the counter anion.³³ Initially, we attempted to determine the crystal structure of complex **1**. For this purpose, we diffused toluene into an acetonitrile solution of the complex to grow single crystals of **1**. In our best attempt, we obtained a structure for **1** in which the position of the diiron core, the ligand scaffold, and the triflate counter anion are well defined. However, the propionate groups are highly disordered, making it impossible to locate the electron density associated with the propionate side chains. The obtained structure of the $\{\text{Fe}^{\text{III}}_2((\text{Py}_2\text{PhO}_2)\text{MP})\}$ core itself is very similar to that of **1-OAc**, in the case of which a fully solved crystal structure has been reported in the literature.²⁸ However, the structure of the diferrous complex **2-OAc** could not be obtained so far. Conveniently, we can generate **2-OAc** by reduction of **1-OAc** with two equivalents of CoCp_2 , thus allowing us to isolate, crystallize, and structurally characterize **2-OAc** for the first time. By diffusion of hexane into a solution of **2-OAc** in CH_2Cl_2 , orange rod crystals of this complex could be obtained, suitable for diffraction. The crystal structure of **2-OAc** is shown in Figure 7.

Table 1 compares the structural parameters for **1-OAc** and **2-OAc**. Both complexes have very similar structures that feature two six-coordinate iron centers that are connected by the central phenolate unit and the two bridging carboxylate (acetate) ligands. In **2-OAc**, the metal-ligand bonds are all elongated as expected, due to the reduction of the iron centers from +III to +II (see Table 1). In **1-OAc**, the two iron centers are essentially equivalent. Upon reduction to **2-OAc**, the diiron core become much more asymmetric, as evident from the Fe-O(carboxylate) bond distances: whereas these bond lengths are essentially all equivalent in **1-OAc**, they differ by up to 0.1 Å in **2-OAc**. In the reduced complex, each iron has one short and one long Fe-O(carboxylate) bond, which suggests that these bridging ligands can be fluxional in solution. This supports the idea that the iron centers in **2-OAc** could become five-coordinate at room temperature in solution, which would explain the temperature-dependent changes in the absorption spectrum of this compound. In this regard, it should be noted that the absorption spectrum of **2-OAc** in the crystalline form is equivalent to that of the low-temperature form in solution (Figure S4, bottom). This strongly indicates that the low-temperature form of **2-OAc** in solution has a similar structure as the crystal

1
2
3 structure of this complex (Figure 7) with six-coordinate Fe(II) centers and two bridging
4 carboxylate ligands. At room temperature, the Fe(II) centers could then become five-coordinate,
5 as discussed above. This would also explain why the process is fully reversible.
6
7

8 The bonds between the iron centers and the amine ligands are also significantly elongated
9 in **2-OAc** compared to **1-OAc**. Despite the significant elongation of the bonds around the iron
10 centers, the core structure of **2-OAc** remains intact and strongly resembles that of **1-OAc** in our
11 crystal structure as shown in Figure 7.
12
13
14
15

16 17 **3.3 Reaction of 2 with NO gas at room temperature** 18

19 Upon addition of NO gas into the headspace of a dark orange solution of **2**, the solution
20 changes color immediately to red. Notably, the IR spectrum of the resulting reaction product shown
21 in Figure S23 does not show any band associated with an N-O stretch (for high-spin {FeNO}⁷
22 complexes, the N-O stretch is usually observed in the 1700 – 1800 cm⁻¹ range¹⁵). We therefore
23 conducted an IR gas headspace analysis of the reaction flask and detected N₂O in high yield (Figure
24 8). Further experiments determined *that N₂O is generated in quantitative yield in the reaction of 2*
25 *with NO gas as shown in Figure S25*. The same result is obtained when complex **2**, generated
26 directly by metalation of H₃[(Py₂PhO₂)MP] with Fe(OTf)₂, is used. Similarly, **2-OAc** generates
27 quantitative amounts of N₂O when reacted with NO gas. *This result shows, for the first time, that*
28 *non-heme diiron sites can in fact directly reduce NO to N₂O from the {FeNO}⁷ redox state*. This
29 provides support for the proposal that FNORs are able to mediate direct NO reduction to N₂O from
30 the diferrous state, without involvement of the flavin cofactor in the reaction. Interestingly, N₂O
31 production by **2** does not require any external source of acid, which confirms our previous result
32 that water formation is not required as a driving force for N₂O generation from NO.⁷ This suggests
33 the formation of a bridging μ-oxo unit, Fe^{III}-O-Fe^{III}, as the direct reaction product besides N₂O.
34 Indeed, the Mössbauer spectrum of the product after the reaction of **2** with NO gas at room
35 temperature shows two quadrupole doublets which are responsible for ~95% of iron, with
36 parameters that are consistent with two antiferromagnetically (AF) coupled high-spin diferric
37 complexes (Figure 9D). The isomer shifts and quadrupole splittings of the two diferric
38 components, 0.53 and 0.80 mm/s (71%) and 0.52 and 1.70 mm/s (22%), respectively, are different
39 from the diferric complex **1** (see Figure 5, top), in agreement with the formation of unique diferric
40 products after the reduction of NO. The two diferric reaction products likely differ in the exact
41
42
43
44
45
46
47
48
49
50
51
52
53
54
55
56
57
58
59
60

1
2
3 ligation of the iron centers, leading to the observed difference in quadrupole splittings. The
4 absorption spectrum of the product shows a shift in the main absorption band from 530 nm in
5 complex **2** to 470 nm with a shoulder at 515 nm, in agreement with the color change from dark
6 orange to red (Figure 10, black). Excitingly, when two equivalents of acetic acid are added to this
7 red product solution, it immediately turns back to the deep blue color of complex **1**. Absorption
8 spectra and mass spectrometry show that the product has indeed turned back into complex **1** after
9 acetic acid addition, supporting the idea that the diferric reaction products contain Fe^{III}-O-Fe^{III}
10 units. Subsequent addition of two equivalents of CoCp₂ regenerates complex **2/2-OAc**, which can
11 be reacted again with NO gas to produce a second, quantitative amount of N₂O as shown by gas
12 headspace IR (Figure S27). Through this experiment we have successfully demonstrated the
13 capability of our complex to carry out the catalytic reduction of NO to N₂O, via the proposed
14 catalytic cycle shown in Figure 11. Note that because CoCp₂ reacts directly with NO gas (see
15 Experimental Section), it is not possible to run the reaction of **1** with NO under catalytic conditions
16 (i.e., with excess CoCp₂, NO and acetic acid).
17
18
19
20
21
22
23
24
25
26

27 The observed reactivity for **2** with NO is in stark contrast to our previously reported
28 complex [Fe₂(BPMP)(OPr)(NO)₂](X)₂, which forms a diferrous dinitrosyl complex that is stable
29 in both the solid and solution state at room temperature.^{16,17} Our results prove that the strongly
30 donating ligand scaffold in **2** is indeed necessary to create more reducing iron centers that are able
31 to promote direct N-N coupling of NO for N₂O formation.
32
33
34
35
36
37

38 **3.4 Reaction of 2 with NO gas at -80 °C**

39 In order to study the mechanism of N₂O generation in more detail, we monitored the reaction of **2**
40 with NO gas at low temperatures (-80 °C) by a combination of spectroscopic and analytical
41 methods. Solution UV-Vis spectroscopy of the reaction mixture at -80 °C (Figure 10, red) shows
42 the appearance of a new absorption band at 430 nm with a shoulder at 525 nm, indicating that the
43 reaction still proceeds, even at this low temperature. Accordingly, solution and gas headspace IR
44 spectroscopy confirm the formation of N₂O under these conditions (see Figure S30 – S33). Further
45 kinetic analysis of the UV-Vis data in Figure 10 (see Figure S6) delivers a $k_{\text{obs}} = 0.1 \text{ s}^{-1}$ for the
46 reaction at -80 °C. Curiously, however, the maximum yield of N₂O at -80 °C is only about 10 –
47 30% (depending on the exact experimental conditions), even when the reaction mixture is kept for
48 90 minutes (note that there are no more changes in the UV-Vis spectrum past ~30 minutes reaction
49
50
51
52
53
54
55
56
57
58
59
60

1
2
3 time). We then further analyzed the reaction mixture at -80 °C after the “steady state” was reached
4 (no more spectral changes). At this point, low-temperature IR spectroscopy shows two bands at
5 1726 and 1707 cm^{-1} (see Figures 12, S29 and S30), which indicates the presence of $\{\text{FeNO}\}^7$
6 complexes in solution as potential intermediates of the reaction. Electron paramagnetic resonance
7 spectroscopy (EPR) reveals two signals at $g_{\text{eff}} = 3.94$ (major component) and $g = 2.01$ (minor
8 species; see Figure S18); however, double integration of the spectrum reveals that these signals
9 correspond to only ~5% of total iron. Mössbauer spectroscopy indicates the presence of at least
10 three distinct Fe-species in the reaction mixture at -80 °C. The 4.2K / 53mT spectrum (Figure 9A)
11 shows a quadrupole doublet associated with the diferrous precursor ($\delta = 1.25$ mm/s, $\Delta E_Q = 3.01$.
12 mm/s, 34% red line), a quadrupole doublet with parameters indicative of the EPR-silent
13 $[\{\text{FeNO}\}^7]_2$ complex ($\delta = 0.70$ mm/s, $\Delta E_Q = 1.26$ mm/s, 21%, blue line), and a magnetically split
14 component exhibiting broad absorption features extending from -10 to +10 mm/s (ca 45%
15 intensity). In the 60 K/0 mT spectrum (Figure 9B), the magnetically split component collapses into
16 two quadrupole doublets with parameters typical of high-spin ferric and ferrous iron, suggesting
17 that the broad magnetic component emanates from a mixed-valent $\text{Fe}^{\text{II}}/\text{Fe}^{\text{III}}$ complex ($\delta = 1.23$
18 mm/s, $\Delta E_Q = 2.89$ mm/s, 23%, turquoise line, $\delta = 0.56$ mm/s, $\Delta E_Q = 0.93$ mm/s, 23%, orange line).
19 Additional spectra shown in Figure S42 indicate a ferromagnetically coupled $\text{Fe}^{\text{II}}/\text{Fe}^{\text{III}}$ cluster with
20 an $S_{\text{tot}}=9/2$ electronic ground state. The Mössbauer parameters determined for this species are
21 strikingly similar to those reported previously for $(\text{Et}_4\text{N})[\text{Fe}_2(\text{salmp})_2]$, a similar species with
22 ferromagnetically coupled $\text{Fe}^{\text{II}}/\text{Fe}^{\text{III}}$ centers and the same $S_{\text{tot}}=9/2$.³⁴ This complex is a dimer with
23 two bridging phenolate ligands that connect the two iron centers. This indicates that in our mixed-
24 valent intermediate, additional bridging phenolates might be present, which might then favor the
25 $S_{\text{tot}}=9/2$ ground state. Importantly, this mixed-valent species is distinctly different from the mixed-
26 valent state that is accessible by simple one-electron reduction of **1** and **1-OAc**. The mixed-valent
27 state of **1-OAc** has been reported to have an $S_{\text{tot}}=1/2$ electronic ground state with $J = -5.3$ cm^{-1} ,
28 suggesting a weak AF coupling between the two iron centers.²⁸ Mössbauer spectroscopy of this
29 species shows no magnetically split components in the presence of a magnetic field (as observed
30 for the mixed-valent reaction intermediate), but instead, two sets of quadrupole doublets can be fit
31 that correspond to a high spin ferric ($\delta = 0.53$ mm/s, $\Delta E_Q = 0.96$ mm/s, 50%) and a high spin
32 ferrous ($\delta = 1.13$ mm/s, $\Delta E_Q = 2.86$ mm/s, 50%) center. We expect the mixed-valent form of **1**,
33 when prepared by simple (electro)chemical reduction, to have similar properties (since **1** and **1-**
34
35
36
37
38
39
40
41
42
43
44
45
46
47
48
49
50
51
52
53
54
55
56
57
58
59
60

1
2
3 **OAc** only differ slightly in the nature of the carboxylate bridges). Therefore, the mixed-valent
4 reaction intermediate formed at -80 °C is clearly a distinct species that likely contains phenolate-
5 bridged iron centers.
6
7

8
9
10 These results imply that when the reaction is conducted at -80 °C, complex **2** proceeds with
11 NO binding and N₂O release, but that a significant fraction of the complex is kinetically trapped
12 in off-pathway intermediates, and these species are unable to re-enter the reaction pathway as long
13 as the reaction mixture is kept at -80 °C. This includes the experimentally observed [$\{\text{FeNO}\}^7\}_2$
14 complex, responsible for the observed N-O stretching bands in the low-temperature IR spectra and
15 further identified by Mössbauer spectroscopy (see above), which must be kinetically trapped in a
16 conformation that does not allow N₂O formation to proceed. In this regard, it is interesting to note
17 that the complex using the dinucleating pyrazolate/triazacyclononane hybrid ligand, denoted as
18 $[\text{L}\{\text{Fe}(\text{NO})\}_2(\mu\text{-OOCR})](\text{X})_2$, which contains two orthogonal Fe-N-O units, is unable to produce
19 N₂O upon reduction (in contrast to $[\text{Fe}_2(\text{BPMP})(\text{OPr})(\text{NO})_2](\text{X})_2$, where the Fe-N-O units are in a
20 *cis* position).³⁵ The presence of unreacted diferrous precursor is likely due to the fact that this
21 complex contains six-coordinate Fe(II) centers at low temperature (see above), which lowers their
22 affinity for NO. The formation of the Fe^{II}/Fe^{III} mixed-valent species at low-temperature could be
23 due to redox comproportionation between the Fe^{III}/Fe^{III} reaction product and the precursor **2**, or
24 this species could correspond to the product of oligomerization of the diferric reaction product and
25 the diferrous complex. It is also possible that the reaction proceeds by a different mechanism at
26 low temperature; this point requires further study. We have attempted to isolate the mixed-valent
27 complex (by precipitation) as a solid at -80 °C for further characterization. However, under these
28 conditions, all iron-containing species seem to precipitate, and we were not able to derive further
29 information about the $S_{\text{tot}}=9/2$ intermediate from these mixtures (which also seem to decompose
30 at room temperature, even in the solid state).
31
32
33
34
35
36
37
38
39
40
41
42
43
44

45 Upon warming up of the solution to room temperature, the species observed at low
46 temperature are “activated” and proceed to produce N₂O, leading to a close to quantitative yield
47 of N₂O as determined by IR gas headspace analysis (see Figure S26). Curiously, the diferric
48 product obtained in this way differs slightly (by UV-Vis and Mössbauer spectroscopy; see Figures
49 9 and 10) from the one obtained when the reaction is run directly at room temperature (see above).
50 As shown in Figure 10, when the reaction is run at room temperature, the product shows a broad
51 absorption band at 470 nm with a shoulder at 515 nm, and no discernible intermediate it detected
52
53
54
55
56
57
58
59
60

1
2
3 during the reaction. At low temperature, an absorption band at 430 nm appears first (see above),
4 and upon warming to room temperature, this band disappears and new features, which resemble
5 the absorption features of the room temperature product, appear at 470 nm with a shoulder at 515
6 nm (see Figure S7 and S9). When the low-temperature reaction mixture is warmed up to room
7 temperature, the Mössbauer spectrum reveals again two diferric products (~80% total iron, see
8 Figure 9C) with parameters typical for AF coupled high-spin Fe^{III}/Fe^{III} complexes. Here, the two
9 components show isomer shifts and quadrupole splittings of 0.53 mm/s and 0.82 mm/s (53%) and
10 0.51 mm/s and 1.64 mm/s (22%), respectively. Hence, the same products are formed as in the room
11 temperature reaction, but in a different ratio (which explains the slight differences in the absorption
12 spectra of the warmed up low-temperature and the room temperature products). As mentioned
13 above, these results indicate that the diferric product exists in the form of different coordination
14 isomers with slightly different properties.
15
16
17
18
19
20
21
22
23
24
25

26 **3.5 The nature of the $[\{\text{FeNO}\}_7]_2$ Intermediate observed at low temperature**

27 The observation of the two IR bands at 1726 and 1707 cm⁻¹ (Figure S31), which belong to
28 the $[\{\text{FeNO}\}_7]_2$ intermediate observed by Mössbauer spectroscopy and shown to be EPR silent
29 (see above), indicates that the reaction of **2** with NO proceeds via the formation of a diferrous
30 dinitrosyl intermediate, similar to the mechanism proposed for FNORs by Kurtz and coworkers.¹²
31 However, isolation and further characterization of this species have proven to be challenging. We
32 therefore used DFT calculations, which have proven to be effective at predicting structural
33 parameters and vibrational properties of non-heme (hs) iron-nitrosyl complexes,^{18,36,37} to gain
34 further insight into the properties of this species. Based on our previously obtained crystal structure
35 of $[\text{Fe}_2(\text{BPMP})(\text{OPr})(\text{NO})_2](\text{BPh}_4)_2$, we constructed an analogous model,
36 $[\text{Fe}_2((\text{Py}_2\text{PhO}_2)\text{MP})(\text{OPr})(\text{NO})_2]$, and then optimized the structure of this species in the AF coupled
37 state using BP86/TZVP.³⁸⁻⁴¹ The fully optimized structure of this complex is shown in Figure 13.
38 The calculations predict the N-O stretching frequencies for this structure to be $\nu_{\text{sym}}(\text{N-O}) = 1723$
39 cm⁻¹ and $\nu_{\text{asym}}(\text{N-O}) = 1678$ cm⁻¹, respectively, which is in good agreement with our experimental
40 observations. This result therefore supports our conclusion that the two IR bands at 1726 and 1707
41 cm⁻¹ observed by IR spectroscopy correspond to the dinitrosyl species observed by Mössbauer
42 spectroscopy, and that this is indeed a diferrous dinitrosyl intermediate. However, it should be
43 noted that the intermediate observed by Mössbauer spectroscopy is unable to mediate N₂O
44
45
46
47
48
49
50
51
52
53
54
55
56
57
58
59
60

1
2
3 formation (at low temperature), and hence, the two Fe-N-O units are probably not coplanar in this
4 structure. Since the available information about this intermediate is limited, we did not attempt
5 further calculations on structural isomers of $[\text{Fe}_2((\text{Py}_2\text{PhO}_2)\text{MP})(\text{OPr})(\text{NO})_2]$.
6
7

8 Compared to our previous model complex $[\text{Fe}_2(\text{BPMP})(\text{OPr})(\text{NO})_2](\text{X})_2$, which shows the
9 N-O stretch at 1765 cm^{-1} , the low-temperature intermediate observed here has distinctively lower
10 N-O stretching frequencies, which is in agreement with the idea that $[(\text{Py}_2\text{PhO}_2)\text{MP}]^{3-}$ is a stronger
11 donating ligand than $[\text{BPMP}]^-$. This trend can be explained with the triplet NO^- ligand being
12 predominantly a π -donor from its singly-occupied π^* orbitals in these types of complexes (which
13 are best described as $\text{Fe}(\text{III})\text{-NO}^-$).^{42,43} Here, more electron-rich iron centers show **reduced** charge
14 donation from the NO^- ligand, leading to an increase in the electron density in the π^* orbitals of
15 NO^- , and correspondingly, a decrease in the N-O stretch. This effect further reduces the covalency
16 of the Fe-NO bond, and hence, weakens this bond (and lowers the Fe-NO stretch). The lower N-
17 O stretching frequencies for the low-temperature $[\{\text{FeNO}\}^7]_2$ intermediate observed here
18 (compared to the $[\text{BPMP}]^-$ complex), in combination with our DFT results, are therefore again
19 consistent with the formation of a dinitrosyl complex of type “ $[\text{Fe}_2((\text{Py}_2\text{PhO}_2)\text{MP})(\text{OPr})(\text{NO})_2]$ ”
20 in our experiments. As shown recently, N-N bond formation constitutes the key energy barrier for
21 the reduction of NO to N_2O by non-heme diiron sites;¹⁸ thus, weakening of the Fe-NO bonds in
22 the presence of a strongly donating coligand is in fact advantageous for NO reduction. As the
23 result, the highly donating ligand used here is suitable for allowing for the *direct reduction* of NO
24 to N_2O , without the need to add any extra reducing equivalents to activate the $\text{hs-}\{\text{FeNO}\}^7$ units.
25
26
27
28
29
30
31
32
33
34
35
36
37
38
39

40 **4. Conclusions**

41
42 In conclusion, the direct reduction of NO to N_2O by a diferrous diiron complex was achieved
43 here for the first time, using the new model complex $[\text{Fe}_2((\text{Py}_2\text{PhO}_2)\text{MP})(\text{OPr})_2](\text{OTf})$. Although
44 previous work on $[\text{Fe}_2(\text{BPMP})(\text{OPr})(\text{NO})](\text{X})_2$ ($\text{X} = \text{BPh}_4^-, \text{OTf}^-$) has shown that reduction of
45 non-heme diiron dinitrosyl complexes induces fast and efficient N-N coupling and N_2O
46 generation,^{16,17} our new results demonstrate that this is **not** a requirement for N_2O production. In
47 fact, *we show here that via tuning of the iron redox potential, the direct pathway for NO reduction*
48 *can be activated*. In comparison to our previously reported model complex,
49 $[\text{Fe}_2(\text{BPMP})(\text{OPr})_2](\text{OTf})_2$, the redox potentials of $[\text{Fe}_2((\text{Py}_2\text{PhO}_2)\text{MP})(\text{OPr})_2](\text{OTf})$ are shifted
50
51
52
53
54
55
56
57
58
59
60

1
2
3 negatively by about 1 V, which was accomplished by the simple substitution of a pyridine ligand
4 with a phenolate group at each iron center. This large negative shift in potential makes the Fe^{III}/Fe^{III}
5 redox state of the dimer accessible, thus allowing the reaction to go forward by oxidizing the diiron
6 core by two electrons. Importantly, we were able to demonstrate the ability of this model complex
7 to perform multiple turnovers of (quantitative) NO reduction in the presence of acetic acid, which
8 mimics the reactivity of the enzyme. Despite the lack of structural characterization, our results
9 further indicate that the product of NO reduction is a bridging diferric oxo product.

10
11 In summary, our results provide direct support for the recent proposal that FNORs mediate
12 NO detoxification via direct NO reduction by their diferrous active sites, without the involvement
13 of the flavin cofactor in the reaction.¹³ In the protein, a fine tuning of the redox potential of the
14 diiron active site could be accomplished by the electrostatic environment of the diiron core,
15 hydrogen bonding, etc., as demonstrated for blue copper proteins.⁴⁴ Finally, our results show that
16 N-N bond formation by **2** proceeds with a very small activation barrier, allowing the reaction to
17 proceed, even at -80 °C. The direct reduction mechanism is therefore a surprisingly facile pathway
18 for NO reduction to N₂O, if the diiron core has the “right” redox potentials. Further work will now
19 focus on identifying the precise nature of the intermediates observed at low temperature, and on
20 determining the exact redox potentials needed to activate the direct reduction pathway of NO.
21
22
23
24
25
26
27
28
29
30
31
32
33

34 ASSOCIATED CONTENT:

35 **Supporting Information:**

36
37
38 The Supporting Information is available free of charge at _____ and contains information on the
39 following: UV-Vis, FT-IR, EPR, CV, NMR, Mössbauer spectra, X-ray crystallography and DFT-
40 optimized coordinates. Supplementary crystallographic data can be found at CCDC deposition
41 #1850172 and can be obtained free of charge.
42
43
44
45

46 AUTHOR INFORMATION:

47 **Corresponding Author**

48
49
50
51 *E-mail: lehnertn@umich.edu
52

53 **Funding Sources:**

54
55 National Science Foundation
56
57
58
59
60

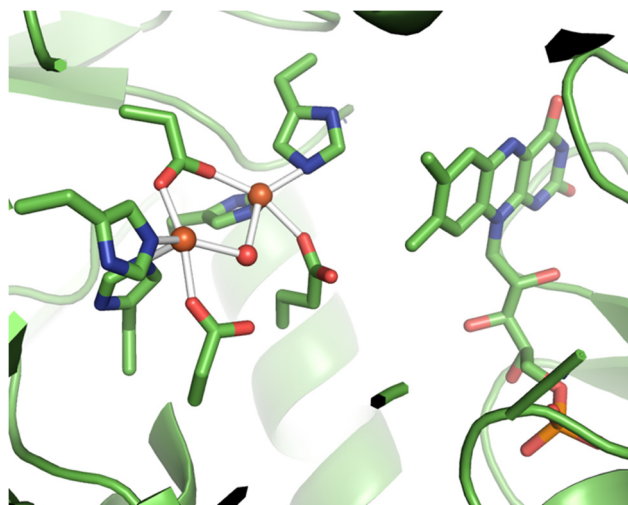
1
2
3 **Notes:**
4

5 The authors declare no competing financial interest
6

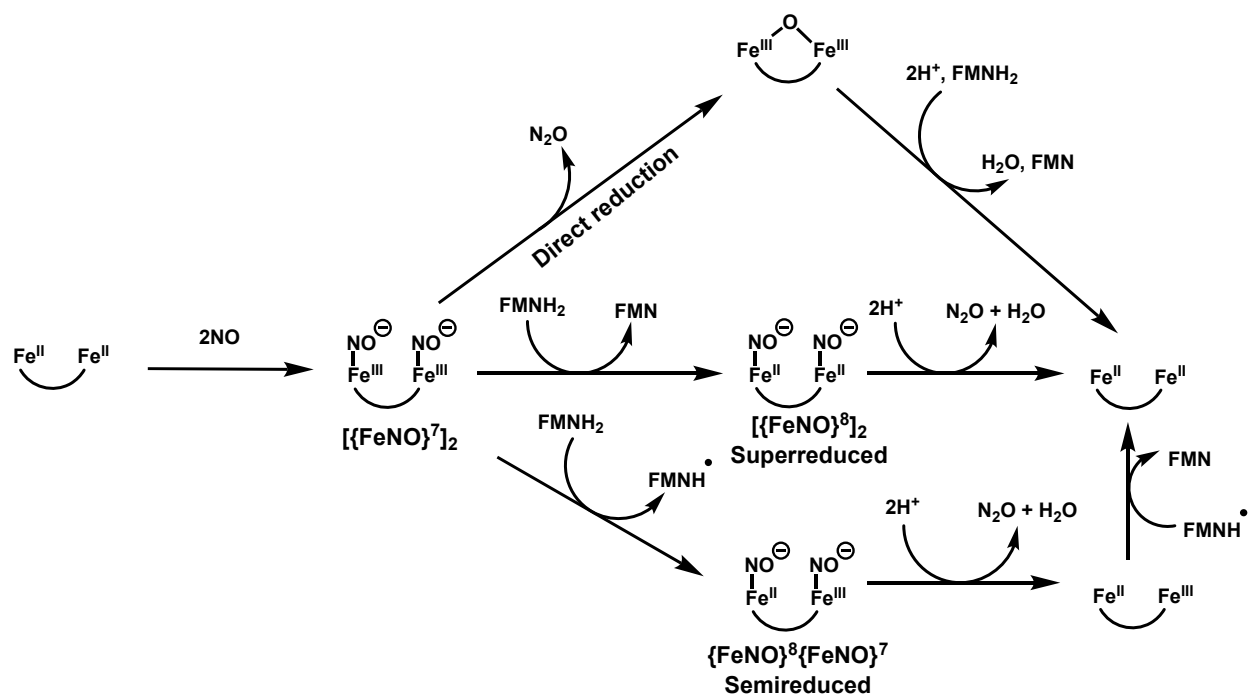
7
8 ACKNOWLEDGMENT:
9

10 This work was supported by the National Science Foundation (CHE-1608331 to NL). We
11 acknowledge Dr. Jeff Kampf (University of Michigan) for X-ray crystallographic analysis of 2-
12 **OAc**, and funding from NSF grant CHE-0840456 for X-ray instrumentation.
13
14
15
16
17
18
19
20
21
22
23
24
25
26
27
28
29
30
31
32
33
34
35
36
37
38
39
40
41
42
43
44
45
46
47
48
49
50
51
52
53
54
55
56
57
58
59
60

1
2
3
4
5 **Figures and Table:**
6
7



23 **Figure 1.** Crystal structure of the diferrous active site of the *Moorella thermoacetica* FNOR (PDB
24 ID 1YCG), shown with the proximal flavin cofactor.⁹
25



50 **Scheme 1.** Different mechanisms proposed for the reduction of NO to N₂O by FNORs. Top: **direct**
51 **NO reduction** pathway observed in FDPs by Kurtz et al., showing that the redox cofactor FMN
52 is only important to re-reduce the enzyme active site after turnover.¹³ Middle: **Superreduced**
53 pathway that requires two equivalents of electrons from the FMNH₂ cofactor to start the N-N
54 coupling reaction. Bottom: **Semireduced** pathway that requires one equivalent of electrons from
55 the FMNH₂ cofactor.
56

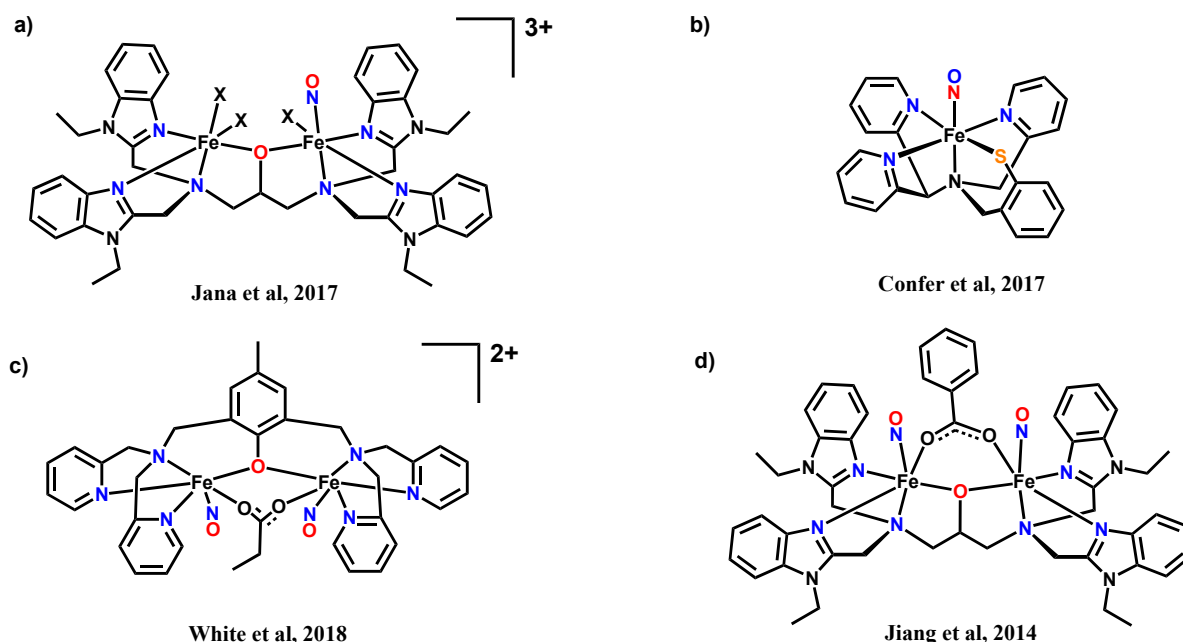


Figure 2. Mono- and diiron nitrosyl model complexes. **A:** A diiron mononitrosyl complex obtained by reacting the precursor, $[\text{Fe}_2(\text{N-Et-HPTB})(\text{CH}_3\text{COS})](\text{BF}_4)_2$, with $(\text{NO})(\text{BF}_4)$. X are solvent molecules $((\text{CH}_3)_2\text{NCHO})$.¹⁹ **B:** An $\{\text{FeNO}\}^8$ complex using the N3PySH ligand scaffold that decays to form N_2O .²⁰ **C:** Our diiron dinitrosyl complex that can form N_2O upon reaction with 1 eq. of CoCp_2 .¹⁷ **D:** A dinitrosyl complex that undergoes Fe-NO bond scission under light illumination to generate N_2O .⁴⁵

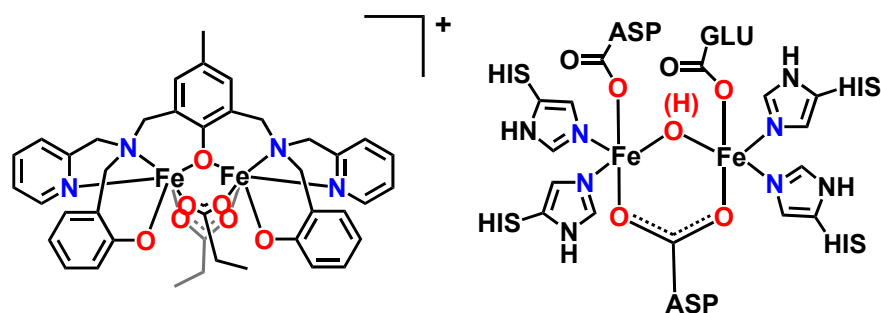
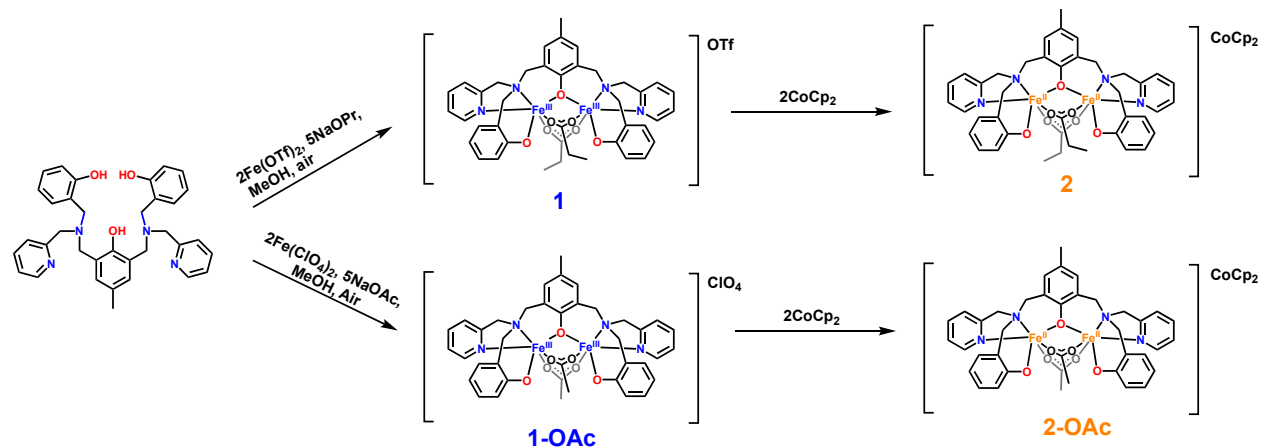
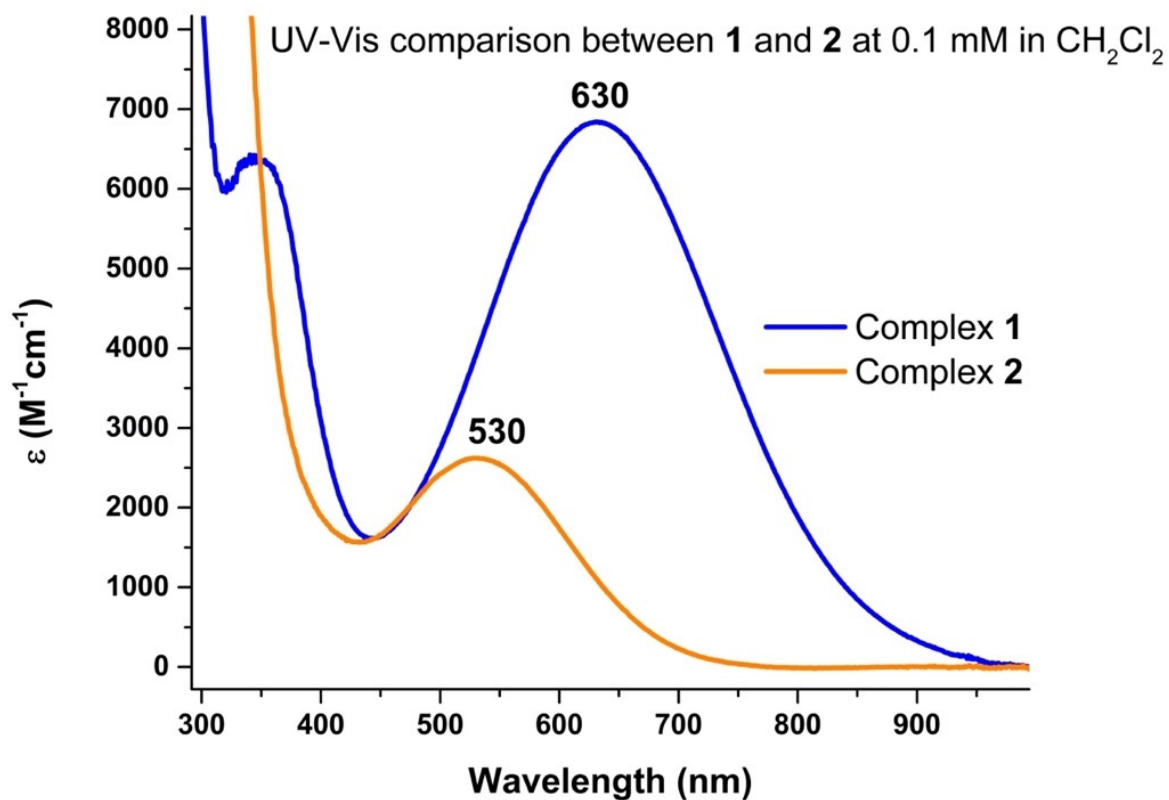


Figure 3. Left: Complex 1. Right: Simplified drawing of the active site of FNORs.⁹



23 **Scheme 2.** Synthesis of **1**, **1-OAc**, **2**, and **2-OAc**.



54 **Figure 4.** Absorption spectra of complexes **1** and **2** in dichloromethane at 0.1 mM concentration
55 at room temperature.

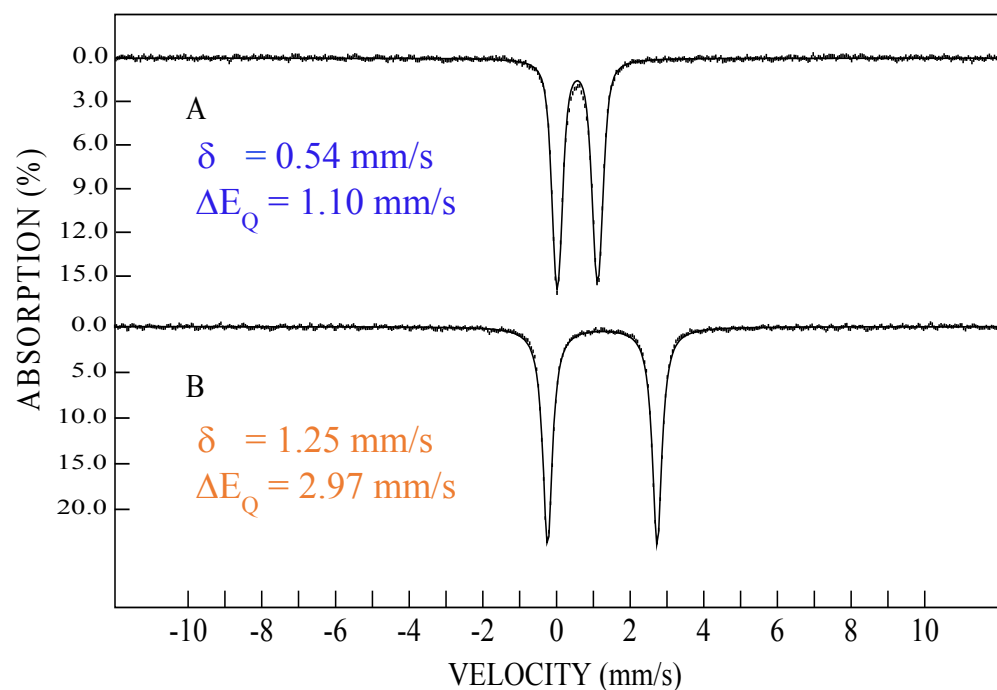


Figure 5. 4.2 K/53 mT Mössbauer characterization of complexes **1** (A, top) and **2** (B, bottom). The solid lines overlaying the experimental data are simulations using the parameters quoted in the main text.

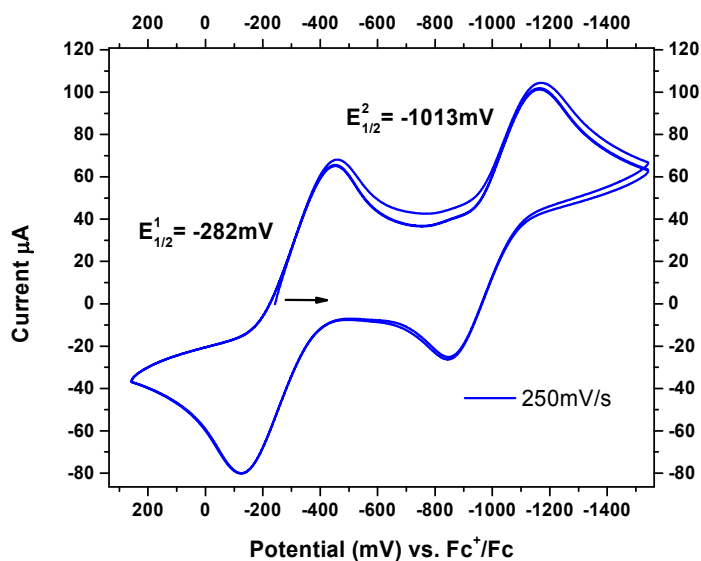


Figure 6. Cyclic voltammogram showing the reversible reduction of **1** in CH_2Cl_2 at 5 mM concentration with 0.1 M tetrabutylammonium trifluoromethanesulfonate used as the electrolyte. Potentials are referenced to a Fc/Fc^+ standard. The experiment was carried out by scanning negatively from the open circuit potential.

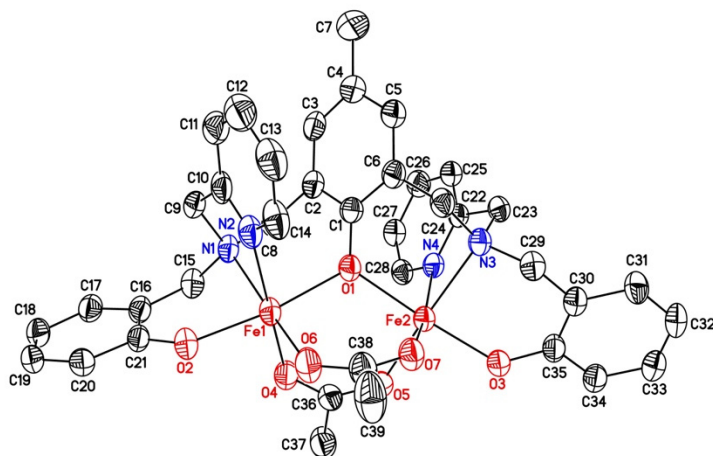
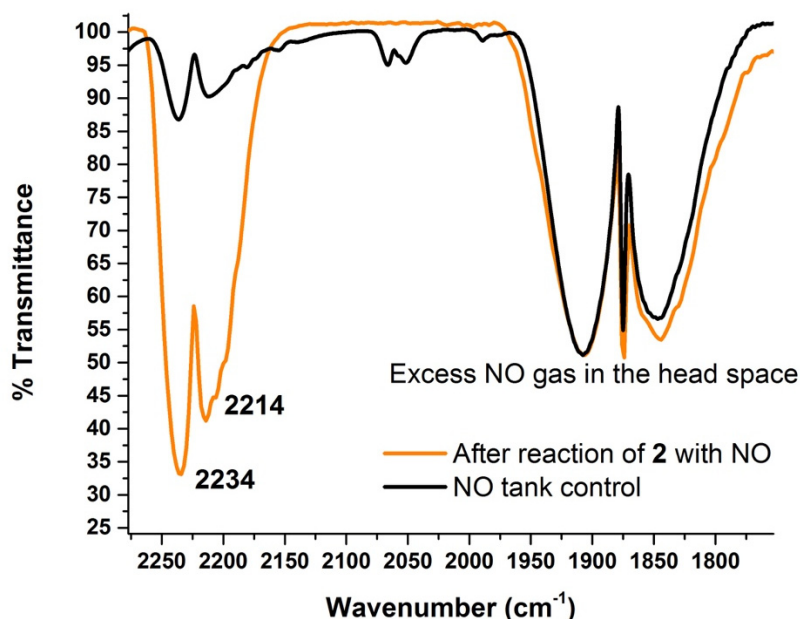


Figure 7. Crystal structure of **2-OAc**, obtained from diffusion of hexane into a saturated solution of **2-OAc** in dichloromethane. The numbering scheme is similar to that reported for the crystal structure of **1-OAc** for better comparison. Solvent molecules, the CoCp_2^+ counter cation, and hydrogen atoms have been omitted for clarity.

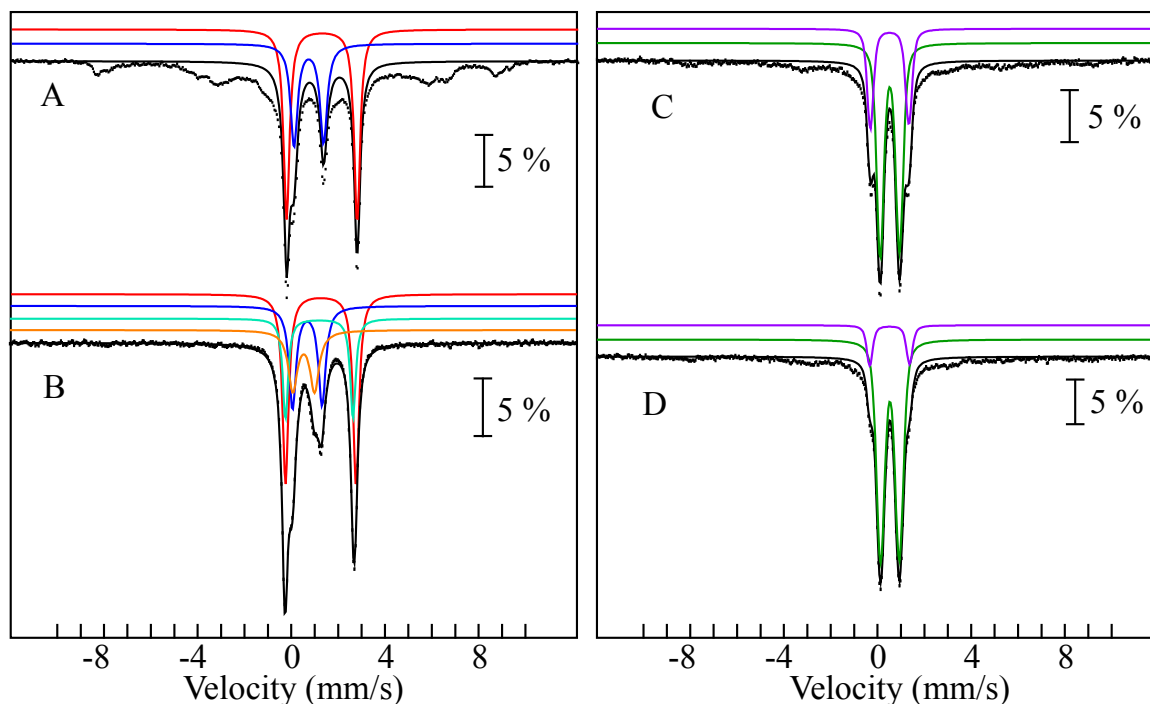
Table 1. Structural comparison between **1-OAc** and **2-OAc**. Values are listed in Å and deg.

Structure	1-OAc (ref. 27)	2-OAc ^a
Fe1-O1	2.054	2.1
Fe2-O1	2.055	2.077
Fe1-Fe2	3.528	3.572
Fe1-O1-Fe2	118.34	117.57
Fe1-N1	2.179	2.247
Fe2-N3	2.169	2.253
Fe1-N2	2.134	2.22
Fe2-N4	2.127	2.253
Fe1-O4	1.965	2.143
Fe2-O5	1.993	2.093
Fe1-O6	1.98	2.107
Fe2-O7	1.956	2.188

^a This work.

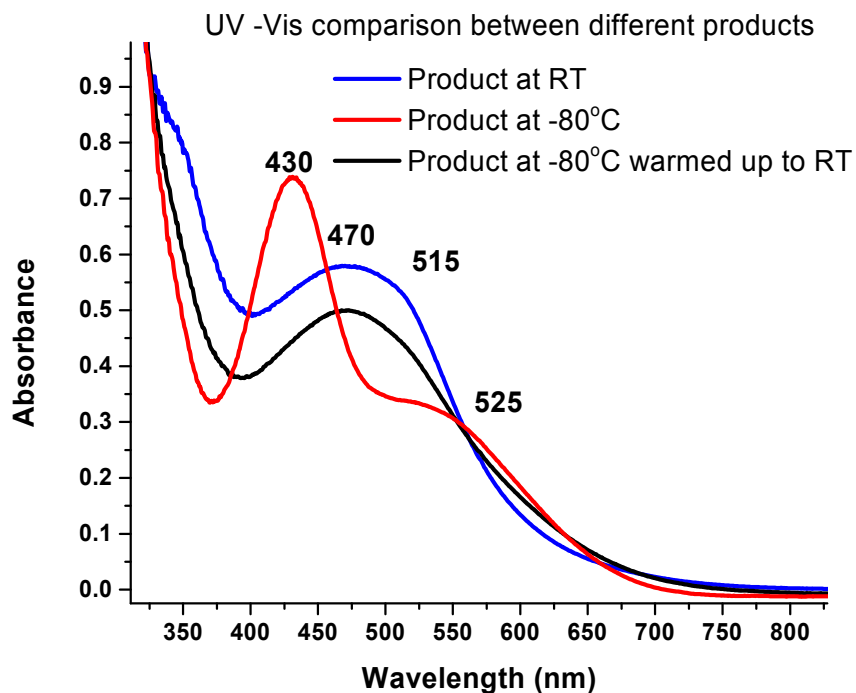


24 **Figure 8.** IR gas headspace detection of N₂O at room temperature (RT), showing the prominent
25 N-N stretch of N₂O at 2234 and 2214 cm⁻¹, which is used to quantify N₂O production.
26



51 **Figure 9.** Mössbauer spectra of a sample of **2** reacted with NO gas at -80 °C for 60 min, recorded
52 at 4.2 K/53 mT (A) and 60 K/0 mT (B). (C) 4.2 K/53 mT spectrum of a duplicate sample of (A),
53 after warming to RT. Simulation parameters: $\delta = 0.53$ mm/s, $\Delta E_Q = 0.82$ mm/s, 53%, green line
54 and $\delta = 0.51$ mm/s, $\Delta E_Q = 1.64$ mm/s, 22%, purple line. (D) 4.2 K/53 mT spectrum of a sample of
55 **2** reacted with NO gas at RT for 15 min. Simulation parameters: $\delta = 0.53$ mm/s, $\Delta E_Q = 0.80$ mm/s,
56

1
2
3 71%, green line and $\delta = 0.52$ mm/s, $\Delta E_Q = 1.70$ mm/s, 22%, purple line. In all spectra, the black
4 line overlaying the experimental data represents the sum of all individual contributions from the
5 fit. Spectral features not captured by the simulation are attributable to the broad, magnetically split
6 features of the $S=9/2$ species.
7
8
9



34
35 **Figure 10.** UV-visible absorption spectra of the reaction product of 0.1 M **2** with excess NO in
36 CH_2Cl_2 at -80°C (red), of this product warmed up to RT (blue), and of the product that is obtained
37 when the reaction is conducted at RT (black).
38
39
40
41
42
43
44
45
46
47
48
49
50
51
52
53
54
55
56
57
58
59
60

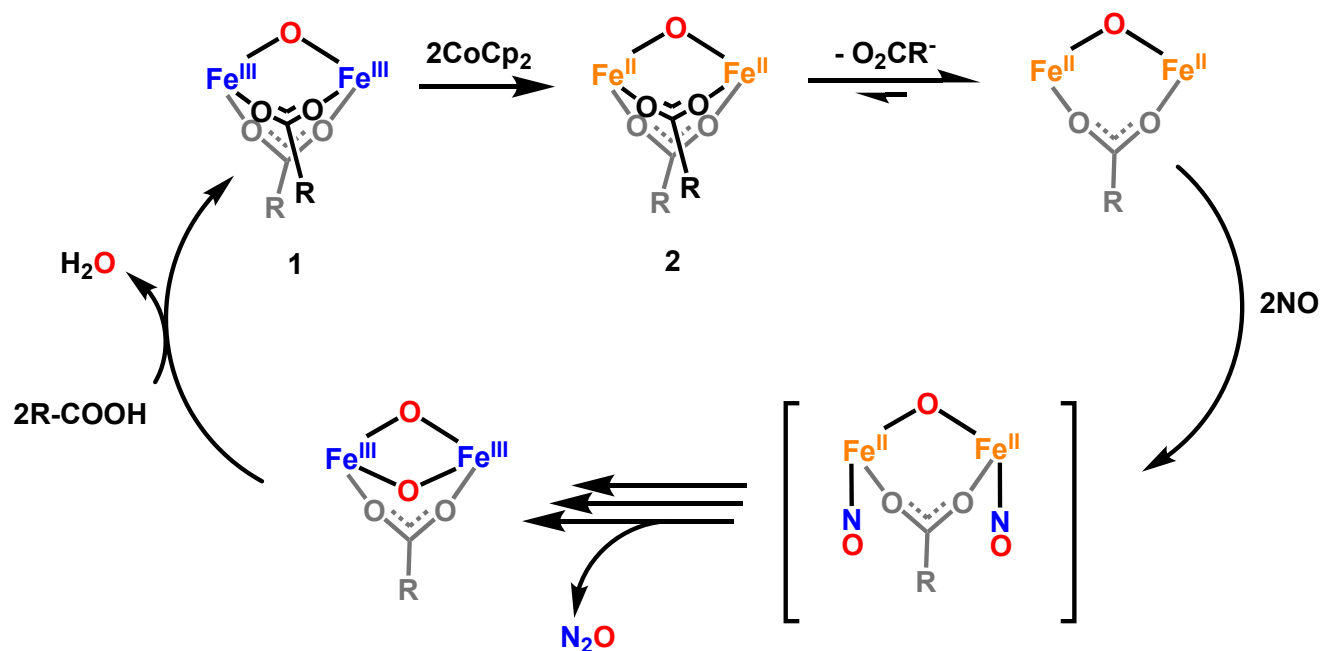
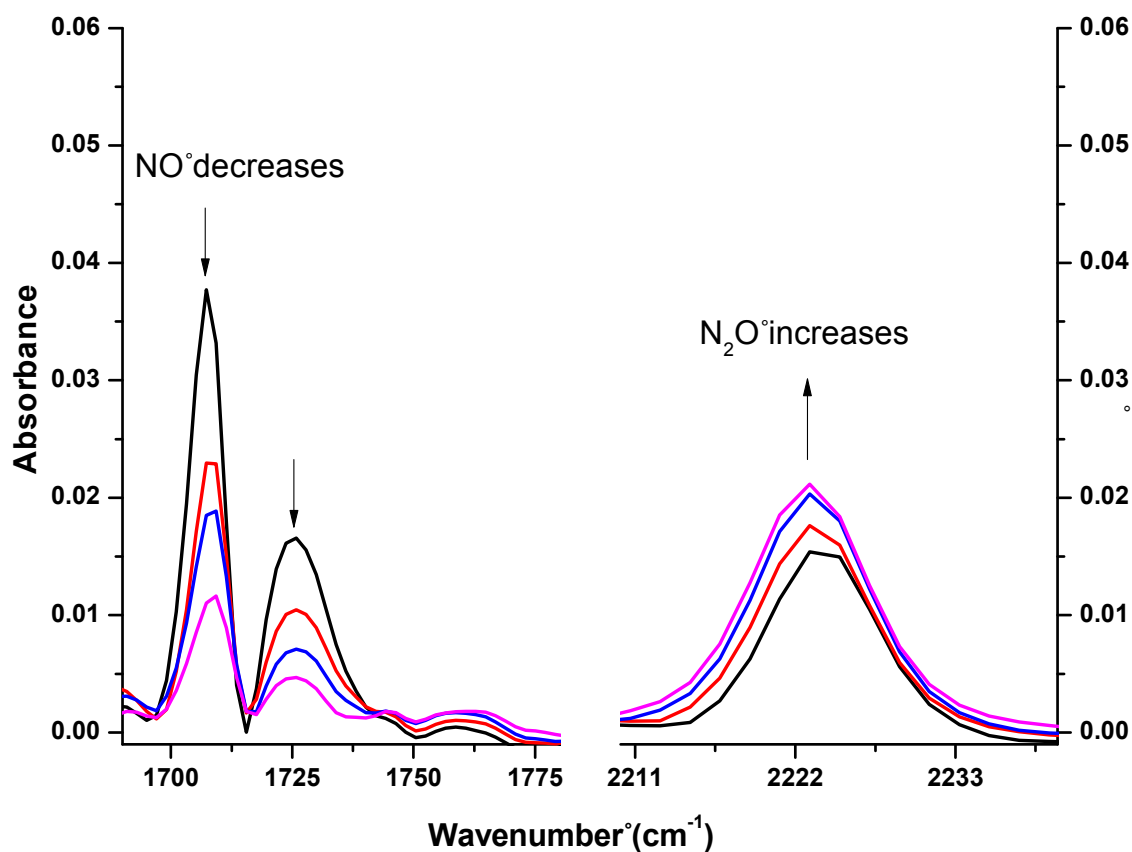
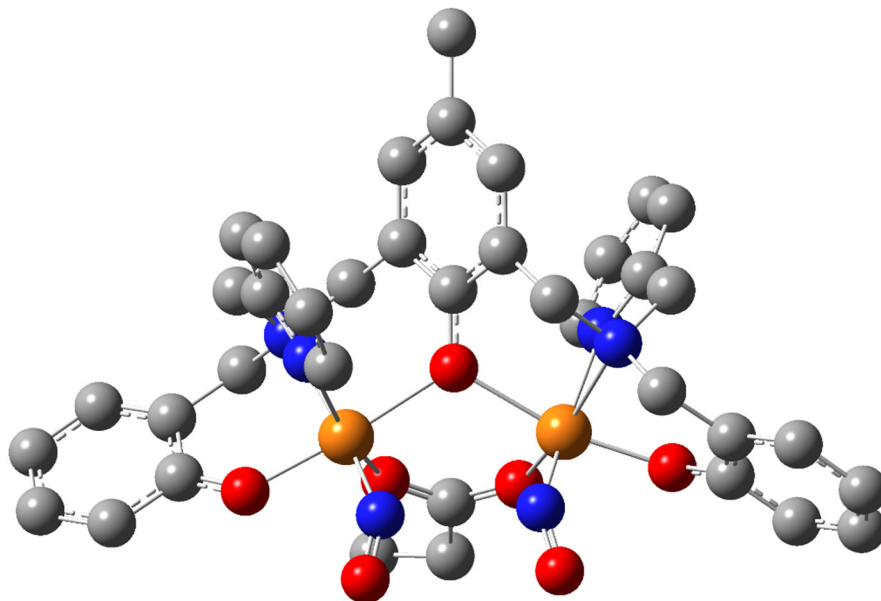


Figure 11. Proposed catalytic cycle of NO reduction at room temperature by complexes **2/2-OAc** in CH_2Cl_2 . Here, the **R** group is a general alkyl chain ($\text{R} = -\text{CH}_2\text{CH}_3$ in complex **2** and $-\text{CH}_3$ in complex **2-OAc**).



1
2
3 **Figure 12.** IR detection of the NO complex observed upon reaction of **2** with excess NO gas in
4 CH₂Cl₂ at -80 °C. Upon warming up, the IR bands of the NO complex decrease in intensity,
5 concomitant with the increase of the N₂O band.
6



28 **Figure 13.** DFT-optimized structure (BP86/TZVP) of the proposed diferrous dinitrosyl
29 intermediate formed at -80 °C. The spin densities are calculated to be about -3 and +3 for each iron
30 center and about +0.5 and -0.5 for each NO ligand. The calculated stretching frequencies of the N-
31 O units are $\nu_{\text{sym}}(\text{N-O}) = 1723 \text{ cm}^{-1}$ and $\nu_{\text{asym}}(\text{N-O}) = 1678 \text{ cm}^{-1}$.
32
33
34
35
36
37
38
39
40
41
42
43
44
45
46
47
48
49
50
51
52
53
54
55
56
57
58
59
60

References

1. Lehnert, N.; Berto, T. C.; Galinato, M. G. I.; Goodrich, L. E. In *The Handbook of Porphyrin Science*; Kadish, K. M., Smith, K. M., Guilard, R., Eds.; . *World Scientific: Singapore* **2011**, *14*, 1.
2. Ignarro, L. *Nitric Oxide: Biology and Pathobiology*. *Academic Press: San Diego* **2000**.
3. Wink, D. A.; Mitchell, J. B. Chemical biology of nitric oxide: insights into regulatory, cytotoxic, and cytoprotective mechanisms of nitric oxide. *Free Radical Biol. Med.* **1998**, *25*, 434-456.
4. Stuehr, D. J.; Gross, S. S.; Sakuma, I.; Levi, R.; Nathan, C. F. Activated murine macrophages secrete a metabolite of arginine with the bioactivity of endothelium-derived relaxing factor and the chemical reactivity of nitric oxide. *J. Exp. Med.* **1989**, *169*, 1011.
5. Gardner, A. M.; Gessner, C. R.; Gardner, P. R. Regulation of the Nitric Oxide Reduction Operon (norRVW) in *Escherichia coli* : ROLE OF NorR AND $\zeta 54$ IN THE NITRIC OXIDE STRESS RESPONSE. *J. Biol. Chem.* **2003**, *278*, 10081-10086.
6. Missall, T. A.; Lodge, J. K.; McEwen, J. E. Mechanisms of Resistance to Oxidative and Nitrosative Stress: Implications for Fungal Survival in Mammalian Hosts. *Eukaryot. Cell* **2004**, *3*, 835-846.
7. Sarti, P.; Fiori, P. L.; Forte, E.; Rappelli, P.; Teixeira, M.; Mastronicola, D.; Sancier, G.; Giuffr , A.; Brunori, M. *Trichomonas vaginalis* degrades nitric oxide and expresses a flavorubredoxin-like protein: a new pathogenic mechanism? *Cell. Mol. Life Sci.* **2004**, *61*, 618-623.
8. Kurtz, J. D. M. Flavo-diiron enzymes: nitric oxide or dioxygen reductases? *Dalton Trans.* **2007**, 4115-4121.
9. Silaghi-Dumitrescu, R.; Kurtz, D. M.; Ljungdahl, L. G.; Lanzilotta, W. N. X-ray Crystal Structures of *Moorella thermoacetica* FprA. Novel Diiron Site Structure and Mechanistic Insights into a Scavenging Nitric Oxide Reductase. *Biochemistry* **2005**, *44*, 6492-6501.
10. Weitz, A. C.; Giri, N.; Caranto, J. D.; Kurtz, D. M.; Bominaar, E. L.; Hendrich, M. P. Spectroscopy and DFT Calculations of a Flavo-diiron Enzyme Implicate New Diiron Site Structures. *J. Am. Chem. Soc.* **2017**, *139*, 12009-12019.
11. Enemark, J. H.; Feltham, R. D. Principles of structure, bonding, and reactivity for metal nitrosyl complexes. *Coord. Chem. Rev.* **1974**, *13*, 339-406.
12. Caranto, J. D.; Weitz, A.; Giri, N.; Hendrich, M. P.; Kurtz, D. M. A Diferrous-Dinitrosyl Intermediate in the N₂O-Generating Pathway of a Deflavinated Flavo-Diiron Protein. *Biochemistry* **2014**, *53*, 5631-5637.
13. Caranto, J. D.; Weitz, A.; Hendrich, M. P.; Kurtz, D. M. The Nitric Oxide Reductase Mechanism of a Flavo-Diiron Protein: Identification of Active-Site Intermediates and Products. *J. Am. Chem. Soc.* **2014**, *136*, 7981-7992.
14. Hayashi, T.; Caranto, J. D.; Wampler, D. A.; Kurtz, D. M.; Mo nne-Loccoz, P. Insights into the Nitric Oxide Reductase Mechanism of Flavodiiron Proteins from a Flavin-Free Enzyme. *Biochemistry* **2010**, *49*, 7040-7049.

- 1
2
3 15. Berto, T. C.; Speelman, A. L.; Zheng, S.; Lehnert, N. Mono- and dinuclear non-heme iron–
4 nitrosyl complexes: Models for key intermediates in bacterial nitric oxide reductases. *Coord.*
5 *Chem. Rev.* **2013**, *257*, 244-259.
6
7 16. Zheng, S.; Berto, T. C.; Dahl, E. W.; Hoffman, M. B.; Speelman, A. L.; Lehnert, N. The
8 Functional Model Complex [Fe₂(BPMP)(OPr)(NO)₂](BPh₄)₂ Provides Insight into the Mechanism
9 of Flavodiiron NO Reductases. *J. Am. Chem. Soc.* **2013**, *135*, 4902-4905.
10
11 17. White, C. J.; Speelman, A. L.; Kupper, C.; Demeshko, S.; Meyer, F.; Shanahan, J. P.; Alp, E.
12 E.; Hu, M.; Zhao, J.; Lehnert, N. The Semireduced Mechanism for Nitric Oxide Reduction by Non-
13 Heme Diiron Complexes: Modeling Flavodiiron Nitric Oxide Reductases. *J. Am. Chem. Soc.* **2018**,
14 *140*, 2562-2574.
15
16 18. Van Stappen, C.; Lehnert, N. Mechanism of N–N Bond Formation by Transition Metal–
17 Nitrosyl Complexes: Modeling Flavodiiron Nitric Oxide Reductases. *Inorg. Chem.* **2018**, *57*, 4252-
18 4269.
19
20 19. Jana, M.; Pal, N.; White, C. J.; Kupper, C.; Meyer, F.; Lehnert, N.; Majumdar, A. Functional
21 Mononitrosyl Diiron(II) Complex Mediates the Reduction of NO to N₂O with Relevance for
22 Flavodiiron NO Reductases. *J. Am. Chem. Soc.* **2017**, *139*, 14380-14383.
23
24 20. Confer, A. M.; McQuilken, A. C.; Matsumura, H.; Moënnelocoz, P.; Goldberg, D. P. A
25 Nonheme, High-Spin {FeNO}⁸ Complex that Spontaneously Generates N₂O. *J. Am. Chem. Soc.*
26 **2017**, *139*, 10621-10624.
27
28 21. CrystalClear Expert, 2.0 r16, C. E. Rigaku Americas: 9009, TX, USA; Rigaku Tokyo, 196-
29 8666, Japan, 2014.
30
31 22. CrysAlisPro, 1.171.38.41; Rigaku Americas Corporation: The Woodlands, TX, 2015.
32
33 23. Sheldrick, G. Crystal structure refinement with SHELXL. *Acta Cryst. C* **2015**, *71*, 3-8.
34
35 24. Spek, A. L. *J. Appl. Cryst.* **2003**, 7-13.
36
37 25. Spek, A. L. *Acta Cryst.* **2009**, *D65*, 148-155.
38
39 26. Frisch, M. J.; Trucks, G. W.; Schlegel, H. B.; Scuseria, G. E.; Robb, M. A.; Cheeseman, J. R.;
40 Scalmani, G.; Barone, V.; Mennucci, B.; Petersson, G. A.; Nakatsuji, H.; Caricato, M.; Li, X.;
41 Hratchian, H. P.; Izmaylov, A. F.; Bloino, J.; Zheng, G.; Sonnenberg, J. L.; Hada, M.; Ehara, M.;
42 Toyota, K.; Fukuda, R.; Hasegawa, J.; Ishida, M.; Nakajima, T.; Honda, Y.; Kitao, O.; Nakai, H.;
43 Vreven, T.; Montgomery, J. A.; Peralta, J. E.; Ogliaro, F.; Bearpark, M.; Heyd, J. J.; Brothers, E.;
44 Kudin, K. N.; Staroverov, V. N.; Kobayashi, R.; Normand, J.; Raghavachari, K.; Rendell, A.; Burant,
45 J. C.; Iyengar, S. S.; Tomasi, J.; Cossi, M.; Rega, N.; Millam, J. M.; Klene, M.; Knox, J. E.; Cross, J. B.;
46 Bakken, V.; Adamo, C.; Jaramillo, J.; Gomperts, R.; Stratmann, R. E.; Yazyev, O.; Austin, A. J.;
47 Cammi, R.; Pomelli, C.; Ochterski, J. W.; Martin, R. L.; Morokuma, K.; Zakrzewski, V. G.; Voth, G.
48 A.; Salvador, P.; Dannenberg, J. J.; Dapprich, S.; Daniels, A. D.; Farkas; Foresman, J. B.; Ortiz, J. V.;
49 Cioslowski, J.; Fox, D. J. Gaussian 09, Revision B.01. *Wallingford CT* **2009**.
50
51 27. Krebs, B.; Schepers, K.; Bremer, B.; Henkel, G.; Althaus, E.; Mueller-Warmuth, W.; Griesar,
52 K.; Haase, W. Model Compounds for the Oxidized Uteroferrin-Phosphate Complex with Novel
53 Dinucleating Ligands Containing Phenolate and Pyridine Donors. *Inorg. Chem.* **1994**, *33*, 1907-
54 1914.
55
56 28. Neves, A.; de Brito, M. A.; Vencato, I.; Drago, V.; Griesar, K.; Haase, W. Fe^{III}Fe^{III} and Fe^{II}Fe^{III}
57 Complexes as Synthetic Analogues for the Oxidized and Reduced Forms of Purple Acid
58 Phosphatases. *Inorg. Chem.* **1996**, *35*, 2360-2368.
59
60

- 1
2
3 29. White, C. J.; Speelman, A. L.; Kupper, C.; Demeshko, S.; Meyer, F.; Shanahan, J. P.; Alp, E.
4 E.; Hu, M.; Zhao, J.; Lehnert, N. The Semireduced Mechanism for Nitric Oxide Reduction by Non-
5 Heme Diiron Complexes: Modeling Flavodiiron NO Reductases. *J. Am. Chem. Soc.* **2018**, *140*,
6 2562-2574.
7
8 30. Neves, A.; Aires de Brito, M.; Drago, V.; Griesar, K.; Haase, W. A new asymmetric N₅O₂-
9 donor binucleating ligand and its first Fe^{II}Fe^{III} complex as a model for the redox properties of
10 uteroferrin. *Inorg. Chim. Acta* **1995**, *237*, 131-135.
11
12 31. Gonçalves, V. L.; Vicente, J. B.; Pinto, L.; Romão, C. V.; Frazão, C.; Sarti, P.; Giuffrè, A.;
13 Teixeira, M. Flavodiiron Oxygen Reductase from *Entamoeba histolytica*: MODULATION OF
14 SUBSTRATE PREFERENCE BY TYROSINE 271 AND LYSINE 53. *J. Biol. Chem.* **2014**, *289*, 28260-
15 28270.
16
17 32. Vicente, J. B.; Teixeira, M. Redox and Spectroscopic Properties of the *Escherichia coli*
18 Nitric Oxide-detoxifying System Involving Flavorubredoxin and Its NADH-oxidizing Redox Partner.
19 *J. Biol. Chem.* **2005**, *280*, 34599-34608.
20
21 33. Campbell, V. D.; Parsons, E. J.; Pennington, W. T. Diiron and dicobalt complexes of a
22 phenolate-bridged binucleating ligand with mixed phenolate and pyridine podands. *Inorg. Chem.*
23 **1993**, *32*, 1773-1778.
24
25 34. Surerus, K. K.; Munck, E.; Snyder, B. S.; Holm, R. H. A binuclear mixed-valence
26 ferromagnetic iron system with an S = 9/2 ground state and valence trapped and detrapped
27 states. *J. Am. Chem. Soc.* **1989**, *111*, 5501-5502.
28
29 35. Kindermann, N.; Schober, A.; Demeshko, S.; Lehnert, N.; Meyer, F. Reductive
30 Transformations of a Pyrazolate-Based Bioinspired Diiron–Dinitrosyl Complex. *Inorg. Chem.* **2016**,
31 *55*, 11538-11550.
32
33 36. Soma, S.; Van Stappen, C.; Kiss, M.; Szilagy, R. K.; Lehnert, N.; Fujisawa, K. Distorted
34 tetrahedral nickel-nitrosyl complexes: spectroscopic characterization and electronic structure. *J.*
35 *Biol. Inorg. Chem.* **2016**, *21*, 757-775.
36
37 37. Fujisawa, K.; Soma, S.; Kurihara, H.; Dong, H. T.; Bilodeau, M.; Lehnert, N. A cobalt-nitrosyl
38 complex with a hindered hydrotris(pyrazolyl)borate coligand: detailed electronic structure, and
39 reactivity towards dioxygen. *Dalton Trans.* **2017**, *46*, 13273-13289.
40
41 38. Perdew, J. P. Density-functional approximation for the correlation energy of the
42 inhomogeneous electron gas. *Phys. Rev. B* **1986**, *33*, 8822-8824.
43
44 39. Becke, A. D. Density-functional exchange-energy approximation with correct asymptotic
45 behavior. *Phys. Rev. A* **1988**, *38*, 3098-3100.
46
47 40. Schäfer, A.; Huber, C.; Ahlrichs, R. Fully optimized contracted Gaussian basis sets of triple
48 zeta valence quality for atoms Li to Kr. *J. Chem. Phys.* **1994**, *100*, 5829-5835.
49
50 41. Schäfer, A.; Horn, H.; Ahlrichs, R. Fully optimized contracted Gaussian basis sets for atoms
51 Li to Kr. *J. Chem. Phys.* **1992**, *97*, 2571-2577.
52
53 42. Berto, T. C.; Hoffman, M. B.; Murata, Y.; Landenberger, K. B.; Alp, E. E.; Zhao, J.; Lehnert,
54 N. Structural and Electronic Characterization of Non-Heme Fe(II)–Nitrosyls as Biomimetic Models
55 of the FeB Center of Bacterial Nitric Oxide Reductase. *J. Am. Chem. Soc.* **2011**, *133*, 16714-16717.
56
57 43. Brown, C. A.; Pavlosky, M. A.; Westre, T. E.; Zhang, Y.; Hedman, B.; Hodgson, K. O.;
58 Solomon, E. I. Spectroscopic and Theoretical Description of the Electronic Structure of S = 3/2
59 Iron-Nitrosyl Complexes and Their Relation to O₂ Activation by Non-Heme Iron Enzyme Active
60 Sites. *J. Am. Chem. Soc.* **1995**, *117*, 715-732.

- 1
2
3 44. Hosseinzadeh, P.; Marshall, N. M.; Chacón, K. N.; Yu, Y.; Nilges, M. J.; New, S. Y.; Tashkov,
4 S. A.; Blackburn, N. J.; Lu, Y. Design of a single protein that spans the entire 2-V range of
5 physiological redox potentials. *Proc. Natl. Acad. Sci. U.S.A.* **2016**, *113*, 262.
6
7 45. Jiang, Y.; Hayashi, T.; Matsumura, H.; Do, L. H.; Majumdar, A.; Lippard, S. J.; Moënne-
8 Loccoz, P. Light-Induced N₂O Production from a Non-heme Iron–Nitrosyl Dimer. *J. Am. Chem. Soc.*
9 **2014**, *136*, 12524-12527.
10
11
12
13
14
15
16
17
18
19
20
21
22
23
24
25
26
27
28
29
30
31
32
33
34
35
36
37
38
39

40 **Table of Contents Figure:**
41
42
43
44

